2012

The Influence of Zinc Content, Strain Rate, and Deformation Temperature on the Thermomechanical Compression of Magnesium-Zinc-Cerium Alloys

Andrew Joseph Thome
Lehigh University

The Influence of Zinc Content, Strain Rate, and Deformation Temperature on the Thermomechanical Compression of Magnesium-Zinc-Cerium Alloys.

by

Andrew J. Thome

A Thesis

Presented to the Graduate and Research Committee

of Lehigh University

in Candidacy for the Degree of

Master of Science

in

Materials Science and Engineering

Lehigh University

May 2012

This thesis is accepted and approved in partial fulfillment of the requirements for the Master of Science.

_____
Date

_____
Wojciech Z. Misiolek, Thesis Advisor

_____
Helen M. Chan, Department Chair

ACKNOWLEDGEMENTS

I would like to extend my deepest gratitude to my advisor, Wojciech Misiolek, whom without I would not have been able to pursue a great deal of my career endeavors and graduate experience. I would like to express appreciation to the Loewy Family, who has made a great deal of my studies possible via the funds set forth by the Lowey Family Graduate Student Fellowship and allowed prior research via the Loewy Visiting Professorship.

I am grateful to the United States Automotive Materials Partnership, which has graciously provided Lehigh University and myself with the opportunity to contribute to this collaborative effort. I would especially like to recognize Dr. Alan Luo, and Dr. Joy Foresmark at the General Motors Corporation for their collaboration and guidance with all aspects of our research. I would like to thank Dr. Alejandro Toro at the National University of Colombia for his contributions this project.

I am indebted to Mr. Samuel Lawrence, William Mushock, and Arlan Benscoter who have all provided me with the technical skills necessary to perform my research. My efforts also would not have been possible without the unconditional support extended to me by all the members of the Instituted for Metal Forming who have helped me focus my research and I would especially like to thank J.C. Sabol for his contributions.

I could not have done this without my father, mother, brother, and sister who have all been an integral part to the success of my efforts and who have unreservedly been there for me. Finally I would like to thank Stephanie, whose moral support and encouragement has helped me through even the most arduous times of my career.

TABLE OF CONTENTS

LIST OF TABLES

LIST OF FIGURES

ABSTRACT

A recent focus on environmental preservation has led to a call for increasing in fuel efficiency and the reduction of vehicle emissions. One approach that U.S. automakers intend to take to address this issue is increasing vehicle efficiency through weight reduction. Additionally, a redistribution of the vehicle center of gravity can increase safety through enhanced handling and control. Magnesium is an attractive material due to having the lowest density among engineering materials however its use to date has been hindered by its relatively low ductility, strength, and tendency to exhibit galvanic corrosion. A Mg-Zn-Ce alloy has been developed which greatly reduces these shortcomings and presents itself as an acceptable candidate to lower vehicle front-end weight. Though this alloy system has shown drastic formability increases over pure magnesium and other Mg-based alloy systems, relatively little is understood about the behavior of this system. This study examined the compression behavior of this alloy at different zinc contents, deformation temperatures, and strain rates. It was observed that the lowest zinc content (2 wt.%) was the most formable as it was able to be compressed over the largest range of strain rates and temperatures. Through a metallurgical examination of the raw material and deformed samples it was seen that at low temperatures samples were able to accommodate imposed stress via twinning. High deformation temperatures showed evidence of dynamic recrystallization. An electron microscopy examination showed that there was a large amount of zinc segregation at the grain boundaries, and showed intergranular fracture modes suggesting that zinc increases were detrimental. An EBSD analysis showed randomized as-cast grain orientation, as well as randomly oriented grains in recrystallized regions suggesting heterogeneous texture played a large role in increasing ductility.

1. BACKGROUND

1.1 Motivation

A recent emphasis on environmental sustainability has placed a heightened focus on the reduction of pollution and curtail of non-renewable resource consumption. These driving forces have placed a large need for the automotive manufactures to make formidable steps in the design, development, and implication of innovations associated with the design of their vehicles. Many approaches have already been developed to offer solutions to these new demands and perhaps one of the more widely considered methods has been through weight reduction of vehicles.

Lightweighting automobiles through materials selection poses many potential benefits by lowering powertrain energy demands, however presents the new issue of selecting materials with a high strength-to-weight ratio that are capable of meeting the safety and performance specifications put forth by the industry. Also, previous design modifications have shown that altering front-end design weight can redistribute the center of gravity of the car. By lightweighting the forward portions of the automobile design, the car's center of gravity can be shifted rearward. Effectively, a more posterior orientation of the center of gravity means that handling and vehicle responsiveness can be increased (1).

A proposed solution to reduce current vehicle weight is construction with the use of magnesium alloys. Magnesium, which is considered to be the lightest structural material, promises an ideal weight savings of about 15 percent through replacement of steel and aluminum counterpart materials that are currently used in vehicle designs (2). The United States Automotive Materials Partnership (USAMP) currently projects that

development of novel magnesium components used by the original equipment manufacturer (OEM) could reduce vehicle weight by 500 pounds. Incorporation of magnesium would be seen in instrument panel components, seat frames, and engine cradle sub frames with a particular focus in front end design. At the time of this study, the use of magnesium alloys employed in automotive manufacturing by OEMs only accounts for an average of 12 pounds of vehicle components (1). Development of magnesium to a more suitable stage for production means that it would be able to be incorporated into a larger number of applications, including more design-critical components in the front-end design.

Like most design modifications, increasing the use of pure magnesium in new vehicles imposes new challenges for automotive manufacturers. Among these is the relatively low ductility, lower specific strength compared to conventional materials such as steel, and galvanic corrosion effects (2; 1; 3). As a result, many studies have been conducted in regards to identifying alloying additions as well as classifying the behavior of different binary and ternary alloy systems which will enhance the material performance of pure magnesium. Alloy systems examined to present have included the additions of Zn, Al, Li, Y, Mn, Ce, Nd, and Zr, among others (4; 5; 6). Additions of each alloying elements have targeted the aforementioned issues associated manufacture and use of pure magnesium.

The design of magnesium alloys needs to be such that it is able to show an enhancement of physical properties over pure magnesium systems to be comparable to materials and alloys currently being used. Alloying additions have drastically improved ductility, allowing magnesium alloys to be developed for extrusion and other high-

deformation forming operations alternative to the high pressure die-cast (HPDC) methods used now (1). Some alloy systems have even obtained ultimate tensile strengths high as 450-520 MPa seen in Mg-Zn-Y systems (7).

1.2 Formability Issues

Pure magnesium is crystallogaphically arranged at the atomic level such that it has a hexagonal close packed (HCP) crystal structure (8). Metals of HCP character exhibit a range of specific strengths and more brittle behavior compared to FCC and BCC materials. The reason that these alloys commonly exhibit this behavior is associated with the deformation mechanisms influencing HCP metals (9).

Conventionally during deformation, only two separate slip systems are activated in the HCP configuration. These slip systems are aligned in the $\{0002\}\langle 11\bar{2}0\rangle$ family denoted as the basal slip plane. Additionally, alloys of this character tend toward preferential basal-oriented grain texture (9). These characteristics inhibit the potential for homogenous material deformation due to the fact that five independent systems, which are necessary to satisfy the Von Meises criteria, are not activated (10). Magnesium alloys are only able to accommodate stresses in a basal-aligned structure through twinning. This means that upon application of stress, deformation will be propagated via twins constrained to a single direction depending on the crystal lattice orientation. Consequently, imposed stresses mean a higher frequency of twin plane interfaces will be developed which also provide more sites where failure (via cleavage fracture) can initiate (9; 11).

1.3 Magnesium Alloy Systems

Various magnesium alloy systems have been developed to modify the crystallographic texture and enhance slip system activation for improvements in strength and ductility as compared to the pure magnesium systems. Frequently, ternary systems have been developed in which one alloying element contributes to improvements in ductility behavior while the other enhances strength. The success of any alloy system depends on alloying elements interacting in a manner that undesired, non-coherent binary compounds do not develop (12).

This particular study focuses on the ZExx system which is a ternary alloy composed of magnesium, zinc, and cerium. The interaction of this system is able to be considered as three distinct binary contributors between the Mg-Zn, Mg-Ce, and Zn-Ce systems (13). Typically, zinc additions in magnesium alloys have been accompanied by respectable gains in strength and corrosion resistance at the expense of brittle behavior and grain coarsening. To offset this effect, minor alloying additions of rare earth metals have been found to improve these negative effects thereby enhancing alloy system performance (2; 14; 12).

1.4 Characteristics of the Mg-Zn-Ce System

Prior to the development of the Mg-Zn-Ce ternary alloy, an earlier system based on Mg-Al-Ce was used for augmentation of strength and ductility. In this system, aluminum was the intended to function as a strengthener while cerium provided modification of grain texture to enhance ductility. The issue with this system was that while each of these alloying constituents were capable of altering the mechanical properties of magnesium, aluminum has a high affinity for cerium hence forming a large amount of Al-Ce binary compounds. These interactions led to undesired precipitate

formation as well as cerium alloying constituents being "robbed" from the α-magnesium matrix. To combat this effect, the ZExx system was developed by the General Motors Corporation to replace aluminum with zinc. Zinc exhibits a much lower affinity for cerium as compared to aluminum and therefore preserves a large amount of the already scarce 0.2wt% to contribute to ductility changes (15). Use of zinc in this system boasted comparable strength as compared to aluminum while allowing for neglect of the Zn-Ce isopleth in design.

Juxtaposed to pure magnesium, the ZExx system showed considerable improvements in formability allowing for increased linear extrusion speeds of 20 ft./min and tensile yield strengths as high as 289 MPa. Stiffening effects, believed to be caused by increasing zinc content, manifested as higher yield strengths and lower achievable tensile elongations as the relative amount of zinc increased. Though the understanding of some aspects of this system is still cursory, considerable steps have been made in comprehending the microscopic and macroscopic contributions of alloying elements of this system which lead to these new properties.

1.5 Ductility in HCP systems

Ductility enhancements in HCP structure metals can be primarily achieved through use of one of two mechanisms imposed by alloying additions: 1) reducing the c/a ratio of the crystal lattice, or 2) randomizing grain texture to obtain a weaker basal texture.

As established earlier, the limited ductility of HCP metals can be attributed to a dominance of $\{0002\}\langle 11\bar{2}0\rangle$ slip which does not allow for homogenous deformation due to limited slip plane activation. Drastic increases ductility are in this system are

commonly seen when non-basal twin planes in the <11$\bar{2}\bar{3}$> direction or (c+a) pyramidal slip is activated. Two distinctive basal-type twins exist known as compression and tensile twins which allow hexagonal crystals to deform in each corresponding stress state. In basal slip, compression twins accommodate strains by{10$\bar{1}$1} twins then {10$\bar{1}$2} retwinning. The latter enables extension through {10$\bar{1}$2} twinning (9). Considering twinning and pyramidal-type slip, the latter is the most desirable since it is the only deformation mechanism that provides five independent slip modes necessary for homogenous deformation as previously established (2; 16; 9) (16). A graphic example of each crystal-plane deformation mode in HCP crystals can be seen below in Figure 1

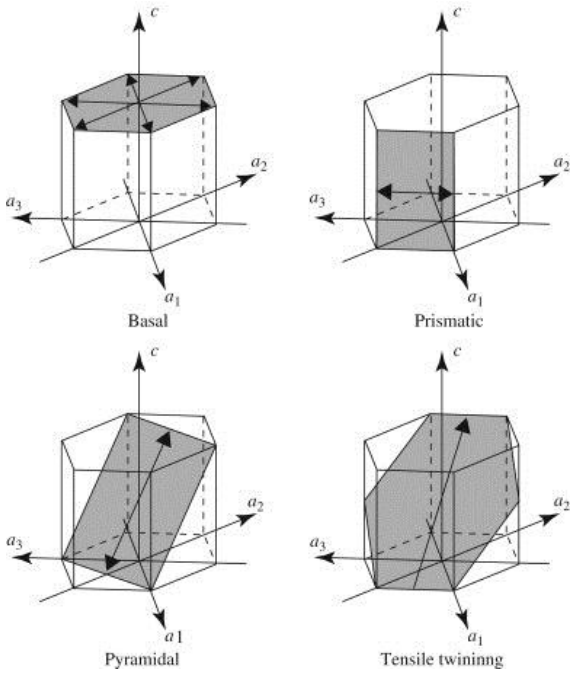

Figure 1: Twinning and slip modes possible in HCP magnesium (17)

Grain randomization and recrystallization functions as a ductility promoter since in some cases it has been associated with weak or non-basal texture responsible for facilitating ductility increases. Previous research by Luo *et al.* examined extruded rods

that experienced some degree of recrystallization at higher linear extrusion speeds. These new, stress-free grains showed weak basal texture (2). Consequently, this more heterogeneous texture was correlated with an increase in percent elongation seen with tensile specimens (16).

Ductility changes can be attributed to this new, non-basal aligned texture which allowed for twinning in new directions. As such, the random texture means that the basal slip mechanism is possible in new directions facilitating material deformation in more orientations. This does not necessarily mean that new pyramidal type slip is activated, rather grain extension via tension twinning is not constrained to a single direction due to grain texture. This has also been suggested that in addition to new extension twin directions, smaller grain boundaries provide more boundary area which allows for grain boundary sliding which occurs in magnesium and its alloys (11). Furthermore, it was proposed that higher extrusion speeds caused more recrystallization, inducing increased ductility (11; 18). Definitive observations have shown that rare earth additions have a textural influence causing transverse direction split texture which increases the lattice's ability to accommodate stress (18). In some instances, processing methods such as equal-channel angular pressing have been used in an attempt to achieve a finer and random grain distribution in these alloy systems (19).

Considering the former ductility enhancement mechanism, reduction of the c/a ratio refers to increasing the match in axis length between the a and c unit cell directions. In the scope of an HCP unit cell, the a-axis direction refers to the direction vector in the $<11\bar{2}0>$ family and the c-axis refers specifically to the [0001] direction. Therefore, reduction of the c/a ratio essentially designates a reduction in the c-axis via vertical

compression of the unit cell (8). By doing such, the critical resolved shear stress (CRSS), which defines the minimum imposed shear stress to initiate deformation, is reduced in pyramidal orientations. A c-axis crystal compression reduces the amount of stress needed to initial these c + a pyramidal slip mechanisms (commonly with a CRSS 100 times higher) than their basal counterparts (2), (11), (16). This reduction in CRSS would mean that slip in these directions becomes much easier, and much more active.

In either enhancement mechanism described, the desired effect is to reduce the necessity to deform only in preferential slip directions thereby causing more isotropic deformation. Studies have also shown that processing at elevated temperature increases the tendency to slip in pyramidal directions due to the addition of activation energy to the system (10).

Cerium has been shown to play a crucial role in contributing to ductility enhancements in the use of magnesium alloys. Studies have targeted even very dilute additions of 0.2 wt.% are sufficient in order to observe considerable improvements over pure magnesium and other Mg-based alloys (2; 16; 11). To date, the contribution of this alloy is not fully understood though it is thought that the presence of Ce precipitates impede grain growth causing grain randomization and refinement during recrystallization and recovery. This grain boundary drag effect is thought to lead to the recrystallization ductility mechanism mentioned earlier.

1.6 Strength modification in HCP systems

Strengthening effects in Magnesium alloy can commonly be attributed by the cessation of basal-type slip through precipitates and solid solution strengthening. In these models, traveling dislocations encounter these precipitate phases and are slowed by having to cut the precipitate. These dislocations are then penalized in the form of higher energies required to form new interfaces between the newly created precipitate surface and matrix material. Likewise, a traveling dislocation will be hindered by local lattice strain fields originating from solid solutes. Such effects lead to an inherent increase in yield and tensile strengths of the alloyed magnesium (20; 21; 22). Several metals have been examined as the strengthener in magnesium alloys, namely Al, Mn, and Zn (16; 2).

In this particular study, zinc has been selected as the strengthening agent. Strength increases through use of this metal have been attributed to a solid solution strengthening, and precipitation hardening which both impede dislocation movement (23). Zinc additions have been shown to have beneficial influences on yield and tensile strengths of up to 96% (2). Unfortunately, there also exists a critical composition and which ZExx alloys become brittle. These effects are still not fully understood but are attributed to an excess of a solid solution strengthening effect (20; 23).

1.7 Thermo-mechanical simulations

Compression testing of metal alloys serves as a good indicator of material formability in production as many deformation processes (e.g. rolling, extrusion, forging) take advantage of compressive forces. Additionally, general mechanical behavior can aide in predicting material behavior in different stress states and loading situations. Mechanical tests in the compressive mode are nearly analogous to tensile loading with the sole exception that the occurrence necking phenomenon and resulting instability that

develops thereafter is not present. While testing in this mode may lack determination of a definitive ultimate tensile strength, it allows for gross deformation of material and classification of behavior over a larger degree of strains (22). Comparative compression techniques allow for an extensive understanding of flow-stress behavior (plastic behavior) and are a good indicator as to the relative formability among various alloys tested under the same conditions.

Process temperatures and deformation rates during manufacturing frequently reach very high rates (on the order of hundreds of meters per second and thousands of degrees) and therefore a fundamental understanding of room temperature behavior is not sufficient. Often, the science of metal forming deviates from theoretical expectations and the most accurate way to classify a system is through *in situ* observation. For this purpose, the Gleeble® 3500 system was used. This particular thermal mechanical simulation system is capable of resistive heating at a rate of 10,000°C/sec and deformation rates of 1m/s (24). These capabilities allow for more realistic modeling of those environments seen in the manufacturing situation.

In the current study, three grades of magnesium alloy, ZE20 (Mg – 2 wt. % Zn – 0.2 wt. % Ce), ZE50 (Mg – 4 wt.% Zn – 0.2 wt. % Ce), and ZE80 (Mg – 8 wt.% Zn – 0.2 wt. % Ce), were compressed at a variety of identical conditions (2). The study focused on the interaction of three variables: zinc content, deformation temperature, and strain rate (defined as the dimensionless parameter which represents the fractional percentage of deformation per second). Of interest were the material structure prior to deformation, material performance during deformation, and the material structure after deformation. This study examined the merit "performance" using the compression flow-

stress behavior of each alloy. Observational metallography was then employed on deformed and undeformed samples to offer an explanation as to the influence of each process parameter.

2. EXPERIMENTAL

2.1 Overview

In order to study and better understand the Mg – Zn – Ce system, thermo mechanical compression tests were performed to observe the resulting flow-stress behavior. The macroscopic scope of this research set out to examine the effect of zinc content on the mechanical performance of each magnesium alloy. This study focused on three specific material chemistries each with a different zinc content, ZE20 (Mg – 2 wt. % Zn – 0.2 wt. % Ce), ZE50 (Mg – 4 wt.% Zn – 0.2 wt. % Ce), and ZE80 (Mg – 8 wt.% Zn – 0.2 wt. % Ce). The specific chemistries of each table can be seen below in Table 1.

Table 1: Elemental compositions in wt.% for ZE20, ZE50, and ZE80 **(2)**

Alloy	Zn	Ce	Mn	Si	Fe	Cu	Ni
ZE20	2.4	0.23	0.02	0.10	<0.005	<0.005	<0.003
ZE50	4.9	0.23	0.02	0.15	<0.005	<0.005	<0.003
ZE80	7.6	0.22	0.04	0.20	<0.005	<0.005	<0.003

Compressions were performed at various temperatures and strain rates to model different process conditions that are seen during deformation processes. Physical deformation tests yielded a wealth of mechanical data, while comparative metallography provided explanations as to the various behavior mechanisms activated in order to facilitate physical deformation.

2.2 Compression Trials

A Dynamic Systems Incorporated (DSI) Gleeble 3500 thermo-mechanical test system offers a very broad array of types of mechanical tests that can be performed on conductive materials. Output parameters range from the development of stress- strain relationships, dilatometry, fatigue, and melting solidification tests (24). In this particular

examination, use of the Gleeble system was attractive due to its ability to operate under a strict control of temperature while being able to achieve a broad range of deformation strain rates.

2.2.1 Test specimens examined

Three, 0.106m diameter billets of ZE20, ZE50, and ZE80 were received in the as-cast condition. Each of these specimens were sectioned and cut into prismatic square sections. These sections were then turned to produce cylindrical test specimens which measured 8mm in diameter by 12mm in length. Spare material was reserved to be used as raw material for comparative metallographic comparisons seen in this study. Test specimen dimensions were devised from manufacturer literature which provides specifications for test-specimen geometry that should be used for each stress mode (24).

2.2.2 Steel sample calibrations

Manufacturer literature suggests that the system is able to achieve heating rates as high as 10,000°C/s and deformation rates as high as 1 m/s. Preliminary verifications and calibration tests were first performed to ensure that the system was capable of operating within the desired conditions of this specific study. For calibration trials which required mechanical deformation of the specimen, a set of Mg-based, AZ31 compression samples of the identical test geometry were used.

2.2.2.1 TEMPERATURE DISTRIBUTION EXAMINATION

As the sample was resistively heated by the Gleeble system, there was a possibility of the existence of an inhomogeneous temperature distribution due to temperature difference contact at the interface between the compression specimens and

the anvil caps. To examine for such a feature, a two-channel thermocouple input was used to examine the differences between temperatures on two discrete points along the length of the specimen. A single ZE50 specimen was used for multiple trials and then discarded in case the repeated thermal cycles had changed the microstructure of the alloy. The sample was held by direct contact via an applied pressure between the two compression anvils. The compression bar was subjected to various heat-and-hold thermal cycles using a heating rate of 5°C/sec and soak time of 2 minutes. Target temperatures of 200°C, 375°C, and 450°C were used. The two-channel temperature output matched within the degree of error of the system and samples were assumed to be homogenously heated for all subsequent trials.

2.2.2.2 THERMOCOUPLE OUTPUT VERIFICATION TRIALS

Temperature verification trials were performed to determine that the thermocouple readings performed by the Gleeble computer system did in fact correspond to the physical temperature of the specimen. In order to test for this, a set of Omegamarker ® high-range temperature sensitive markers were used. A ZE50 scrap sample was set between the grips and allowed heat and soak at 250°C for four minutes. As the sample cooled, markers specifically sensitive to temperatures of 232°C, 204°C, 177°C and 149°C were compared to thermocouple output to ensure validity; results showed that thermocouple output and marker indications agreed.

2.2.2.3 STRAIN RATE ANALYSIS

Verifications were performed to make sure that the Gleeble-jaw articulation speed was capable of achieving the highest strain rate seen in this study, which was 15/s. This verification was done by deforming multiple AZ31 samples at a strain rate of 15/s.

(12mm-long samples were compressed by 6mm in 0.033s). A relationship of jaw displacement vs. compression time was plotted to ensure that such strain rates could be achieved. Based on performance, envelope testing showed that strain rates to 20/s were reliably achievable.

2.2.3 Trial strain rate and temperature selection

Initial test parameters for compression were selected based on extrusion trials which were previously observed and reported in literature. In these trials it was seen that extrusion temperatures of about 400°C were used to successfully extrude magnesium alloys (2). Linear extrudate speeds seen in literature were seen to be near 0.1m/s and hence a target strains of 10/s and 15/s that are typical in magnesium processing were selected (2; 25). Using this basis, a test window was constructed to test at 25°C intervals near a target temperature range of 400°C – 425°C. Strain rates were varied at 5/s intervals with the most tests lying at the target temperature; a condition of .01/s was selected to classify low strain rate behavior. This reasoning was used to develop an original test matrix seen in Table 2.

Table 2: Original test matrix designed featuring intended compression testing parameters for each alloy

Temperature	**Strain Rate (s^{-1})**				
Ambient Temp.	0.01				
200°C	0.01			10	
250°C	0.01		5	10	15
375°C	0.01		5	10	
400°C	0.01		5	10	15
425°C	0.01	1	5	10	15
450°C	0.01		5	10	15

Preliminary testing showed that extreme conditions (high temperatures and high strain rates) of the high-zinc samples commonly failed per the original conditions determined, hence a new test matrix was developed excluding a large amount of these parameters outside of the formability envelope. Based empirically, by using ZE80 to develop an approximate failure envelope, a new test matrix was devised for all alloys and it can be seen in Table 3.

Table 3: Revised test matrix developed after initial testing of high-zinc alloys

Temperature	**Strain Rate (s^{-1})**		
200°C	.01/s	5/s	15/s
375°C	.01/s	5/s	
425°C	.01/s	5/s	15/s

Due to the amount of ZE20 available in this study, the revised test matrix featured less temperature-strain rate couples. Extreme conditions at 425°C and were kept to develop a formability envelope for ZE20 and compare its performance at these parameters to the other alloys. All samples being compressed at a strain rate of .01/s were compressed to a strain of 0.8, all other samples were compressed to a strain of 0.5. These target strains were selected to prevent damage to the Gleeble.

2.2.4 Correction of noise in data output

During preliminary compression trials of samples, it was observed that a sine-form oscillation of stress output was observed when reading force and stress data. It was found that the origin of this issue was due to electronic effects from resistive heating as the sample was deformed. As compression trials commenced, cross sectional area

expansion occurred increasing the contact area between the compression specimen and anvil surface. As a result of this, resistance varied inducting power-cycle lagging allowing electronic noise to be seen in data output by the machine. Two methods were used to correct for this issue:

1) ***Dot.Line acquisition*** was used to obtain data that did not exhibit this behavior. This function only obtained force data points at the amplitude average of heating pulses from the Gleeble; this data was only sampled when there was no oscillation noise.
2) ***Curve smoothing functions*** including moving averages and FFT noise filters were used for data collected prior to acquisition of the dot.line force output.

2.3 Metallographic Analysis

Metallographic preparation of novel alloy systems can prove difficult for many reasons. Each alloy system behaves differently during preparation steps, and can exhibit unexpected responses to different techniques. For example, alloys that are less thermodynamically stable may corrode while using different grinding or polishing media which is not pH balanced. Additionally, the mechanical properties of a specific system have a large influence on the performance of that particular alloy during preparation. Softer or more ductile alloys may be more apt to "smear" or show the appearance that material removal has occurred when deformation has created a faux-smooth surface appearance. Harder alloys may retain scratches from previous preparation steps as they are more resistant to material deformation. Alloy systems that have a high instance of intermetallic compounds, such as the Mg – Zn – Ce system, are subject to particle pull-

out and scratching effects. Preparation for new alloy systems can require a painstaking degree of trial and error before an acceptable procedure can be developed that is acceptable for classification and data collection. Once a sufficient method can be developed, metallography can prove to be an invaluable tool for learning about the phases, deformation behavior, failure mechanisms, and many other properties of a metal.

2.3.1. Metallographic Preparation

Magnesium alloys can provide a large array of issues during preparation due to their tendencies to twin at relatively low stresses. The Mg – Zn – Ce system in particular did not exhibit a strong tendency produce artifact twins during preparation however did exhibit a high degree of chemical activity making it difficult to use with non-neutral pH solutions used in preparation. Additionally, intermetallic pullout was an issue which caused artifact voids and scratching during polishing steps.

2.3.1.1 SECTIONING AND MOUNTING

The ternary Mg – Zn – Ce system exhibits liquidus phase boundaries at relatively lower temperatures so it was important to not cause melting or recrystallization during preparation (14). For this reason, a slow-speed (approximately 300 RPM) diamond cutoff wheel was used to cut metallographic sections with ethanol lubricant. Mounting was done using fast-curing epoxy resin to avoid elevated temperature and pressures used in other mounting techniques which could cause recrystallization and microstructure alteration.

2.3.1.2. GRINDING

The ZExx system contains a large amount of precipitate phases originating from either Mg-Zn or Mg-Ce phases. As a result of this, caution had to be taken to ensure that material removal via grinding techniques is not so harsh as to remove these constituents from the matrix via pullout. Prevention of such effects can be achieved by using a higher-viscosity lubricant during grinding. Commonly a mineral spirits and paraffin wax suspension is used to prevent pullout; use of this solution caused corrosion of the material surface with the ZExx system. In previous literature regarding the preparation of the AM30 and AZ31 alloys B. Gerard showed that use of ethylene glycol produced desired effects and would not corrode Mg-alloys (26).

Grinding steps were selected at intervals that provided small amounts of removal between each step. Samples were ground initially using 240 grit silicon carbide metallurgical paper, then subsequently using 320, 400, 600, 1000, and 1200 grit papers. To prevent oxidation interactions during rinsing steps, ethanol was used in place of water and samples were wiped with cotton swabs, then hot air dried. Samples were ground until scratching from the previous step was no longer visible; for lower grit steps typically one paper was sufficient with 45 seconds of grinding, higher grit steps required two papers (due to paper wear-out) for about 2 minutes of grinding. For each step, approximately 1500N of force was used.

2.3.1.3. POLISHING

Polishing was done in three steps. First a 3-micron diamond suspension was used on an automatic polisher with a Struers MD-MOL™ cloth. This step was followed using a -micron diamond suspension with an automatic polisher and a Struers MD-NAP™

cloth. For each aforementioned step, a pressure of about 2000N was used for about 2 minutes with intermittent applications of Struers DP-Blue™ lubricant. It is important to note that only enough lubricant to eliminate sticking was needed; over-application led to an increased amount of intermetallic pullout. After the 1-micron polishing step, scratching appeared more severe, which is due to elimination of the "smeared" layer formed by subsequent removal steps (26). This effect was eliminated by polishing with a 0.25-micron diamond suspension by hand using medium pressure and a Struers MD-NAP™ cloth for 15 seconds. An ethanol and hot-air dry was used following each polishing step.

2.3.1.4. ETCHING

A comprehensive etching technique was developed in order to adequately reveal grains structure for examination using light optical microscopy (LOM). Samples to be etched were polished to a finish surface of 0.25–micron using diamond particulate. The etching solution used was composed of 4g solid picric acid, 5mL glacial acetic acid, 10mL distilled H_2O, and 100mL ethyl alcohol (190 proof). In order to reduce staining, the etching solution was applied using a saturated cotton swab. Etching was conducted for no more than 2 second intervals after which the surface was immediately purged with ethyl alcohol and hot air dried. These etching intervals were repeated until a preliminary LOM examination showed definitive grain structure. Immediate purging of the surface and use of swab techniques were imperative in order to keep surface staining at a minimum; in the event that the surface was too heavily stained, the surface was re-polished using a 0.25-micron diamond polish and the same etching procedure was conducted again.

2.4 Scanning Electron Microscopy (SEM)

2.4.1 Surface and fractography classifications using SEM

Micrographs were acquired via SEM where standard LOM would not yield the necessary magnifications and resolutions in order to provide sufficient analysis. Namely, imaging via SEM provided to be a powerful tool in the fracture analysis of specimens that failed. The ability to achieve extremely high magnifications was useful for examining fracture surfaces and enabling the explanation of the mode of failure. Classification of general surface morphology was also done using SEM micrographs; zinc and cerium intermetallics could be better resolved using an incident electron beam as these particles were "washed out" by conventional reflective light optical techniques. Phase classification via SEM was made easier by the fact that the constituents in question deviated from the nominal surface profile and therefore could be seen as free–standing structures.

Microscopy studies were done using a Hitachi 4300 field emission SEM and fields of view were taken using PCI image analysis software. For micrograph acquisition, low accelerating voltages and high condenser lens excitations were used.

2.4.2 Energy Dispersive Spectroscopy (EDS)

Energy dispersive spectroscopy (EDS) was used to collect compositional data and verify phase morphology information provided in previous literature (5; 14). The EDAX Genesis EDS system was used with a silicon drift detector. 25 keV accelerating voltages and weakly excited condenser lens settings were used to obtain maximum incident beam strength. Regions of interest were identified where large amounts of clearly-defined precipitate phases were found. Relative phase composition maps were collected using

Mg, Ce, and Zn as the elements of interest. For each map collected, corresponding non-standardized quantitative data was obtained to ensure that the data seen lay within the expected compositional values.

2.4.3 Orientation Mapping via Electron Backscatter Diffraction (EBSD)

*The e*lectron back-scatter diffraction (EBSD) technique was used in order to determine the crystallographic orientation of the material examined in this study. For this examination, the TSL orientation mapping acquisition and TSL orientation mapping analysis software were used in conjunction with an EDAX EBSD detector. In order to run EBSD examinations, a flat surface is necessary in order to ensure an uninterrupted path for the backscatter signal to be collected by the detector, and therefore a unique preparation procedure has to be used.

In initial attempts, samples polished to a 0.25μm finish were used to collect EBSD maps with poor results. The signal generated did not return any distinguishable Kikuchi band patterns because the incident beam was not being effectively diffracted by unique crystal orientations. This effect can be attributed poor surface quality in the form of either excessive topography or the formation of an oxide layer. Use of this light etch improves back-scatter signal (26). Polished samples were chemically prepared by creating a solution of 5mL HNO_3, 15mL glacial acetic acid, 20mL distilled H_2O, and 60mL ethanol and submerging for a duration of 5-10 seconds. Successive attempts to obtain EBSD patterns after this preparation step yielded stronger signal and more successful orientation maps.

Regions of interest used to collect grain texture maps were selected at random while the field of view was at a tilt of 70° and magnification of 100X for coarse-grained structures and 250X for finer-grained structures. The incident electron signal was maximized by using an accelerating voltage of 25keV, gun brightness of 3, weakly excited condenser lens, and the largest aperture setting possible. During map collection, Magnesium was selected as the identification phase as it was assumed that Ce, and Zn existed in precipitates and would not alter the diffraction behavior of the matrix magnesium phase, which was of interest for grain orientation classification.

3. RESULTS

3.1 Preliminary formability assessment (pass/fail analysis)

A preliminary formability assessment analysis was performed for the compressive testing of the ZE20, ZE50, and ZE80 samples progressed. This observation served as the first fundamental merit in determining whether or not an alloy was capable of being successfully deformed at a given set of strain rate and temperature combinations. For the scope of the remaining discussion, the term formability will be defined as the compression bar's ability to withstand given compressive deformation without any apparent failure. Failure will be defined as cracking, fracture, or oxidation which was directly a result of the thermo-mechanical test. As the data obtained is being used to develop an understanding of the flow stress behavior of the Mg – Zn – Ce alloy system is originating from compression test results, the terms compressibility and formability will be used interchangeably.

This examination was rated on a pass or fail basis with an identification of two separate failure modes. The first failure mode was seen as simple surface cracking or a single fracture in which the majority of the specimen remained intact. The second failure mode is identified as complete disintegration of the specimen where compression bars broke into many small granules. Example photographs of these conditions can be seen below in Figure 2a-c.

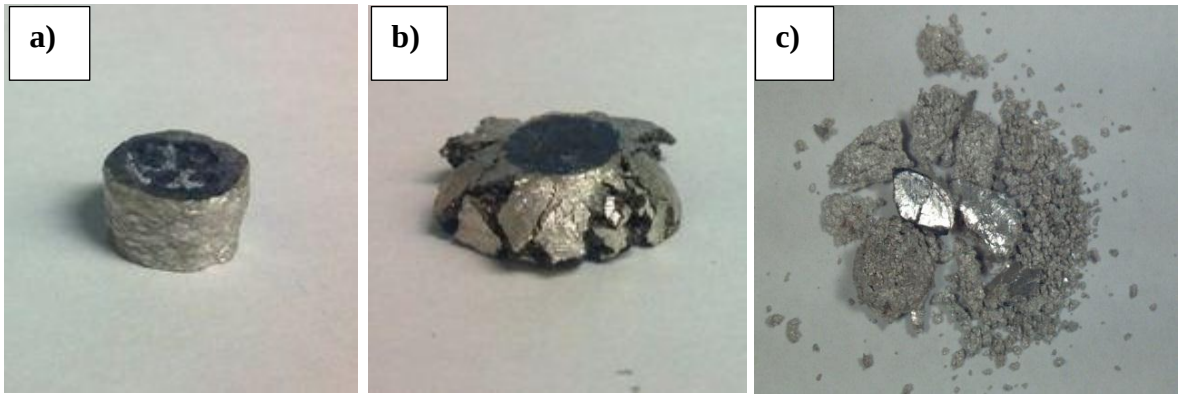

Figure 2: Example of specimen compression outcomes seen in the scope of this study: a) Successful compression with no failure b) Mode I failure with cracking and/or oxidation while some cohesion remains, and c) Mode II failure showing complete disintegration

In order to attempt the fracture mechanics of mode II failures seen in Figure 2c, a fractography analysis was conducted via SEM. The method used in this study will be discussed more in a subsequent section.

The results from the qualitative formability assessment analysis can be seen in respect to the test parameters and alloy zinc content in Table 4 through Table 6

Table 4: Pass/fail results observed for compression of ZE20 samples at various process conditions

Temperature	**Strain Rate**		
	0.01/s	**5/s**	**15/s**
200°C	PASS	PASS	PASS
375°C	PASS	PASS	
425°C	PASS	PASS	PASS

Table 5: Pass/fail results observed for compression of ZE50 samples at various process conditions

Temperature	**Strain Rate**				
	0.01/s	**1/s**	**5/s**	**10/s**	**15/s**
Ambient	$FAIL_I$				
200°C	PASS	PASS	PASS	PASS	PASS
250°C	PASS		PASS	PASS	PASS
300°C				$FAIL_I$	
350°C					
375°C	$FAIL_I$		$FAIL_2$	$FAIL_2$	
425°C	$FAIL_I$	$FAIL_2$	$FAIL_2$	$FAIL_2$	$FAIL_2$

$Fail_I$ Designates mode 1 failure as per Figure 2b
$Fail_2$ Designates mode 1 failure as per Figure 2c

Table 6: Pass/fail results observed for compression of ZE80 samples at various process conditions

Temperature	**Strain Rate**				
	0.01/s	**1/s**	**5/s**	**10/s**	**15/s**
Ambient	$FAIL_I$				
200°C	PASS	PASS	$FAIL_I$	$FAIL_I$	PASS
250°C	$FAIL_I$		PASS	PASS	PASS
300°C				$FAIL_I$	
350°C				$FAIL_I$	
375°C	$FAIL_I$		$FAIL_2$	$FAIL_2$	
425°C	$FAIL_I$	$FAIL_I$	$FAIL_2$	$FAIL_2$	$FAIL_2$

$Fail_I$ Designates mode 1 failure as per Figure 2b
$Fail_2$ Designates mode 1 failure as per Figure 2c

3.2 Gleeble Flow-Stress Output

Gleeble compression trials output a large array of process data including: elapsed time, jaw force, dot-line corrected force, strain, stress, jaw displacement, and up to four channels of thermocouple input. For the accuracy of this data output, strain and stress outputs were not used due to 60 Hz noise from resistive heating as discussed earlier. The dot-line corrected force and jaw displacement were used to directly calculate an engineering stress and engineering strain values. The equation used to calculate engineering stress assumed an initial diameter of 8mm and was

$$\sigma_{eng}\ (MPa) = \frac{Force}{\Pi * (.004mm)^2} * (10^6)$$

Conversely, the engineering strain was calculated directly from the jaw output. The jaw position was zeroed immediately prior to compression and therefore the value of the jaw displacement was assumed to be ΔL, the change in linear length dimension. All bars were assumed to be 12mm in length prior to compression. Engineering strain was calculated using the equation

$$\epsilon_{eng} = \frac{Jaw\ Displacement\ (mm)}{12\ mm}$$

The resulting engineering stress and strain values were then plotted in the compression region only to create a series of flow-stress relationships for ZE20, ZE50, and ZE80. For a controlled comparison of data among the three alloys, only flow-stress diagrams were constructed for those conditions at which all three alloys were tested. Due to the limited amount of ZE20 available for testing, a small array of strain rate and temperatures were examined.

Graphic comparisons of ZE20, ZE50, and ZE80 were created while holding constant temperature and strain rate combinations. Figure 3 through Figure 5 represent the low strain rate testing conditions (0.01/s) tested at temperatures of 200°C, 375°C and 425°C respectively. For the following flow-stress curves, only those marked with "failure" actually failed in compression.

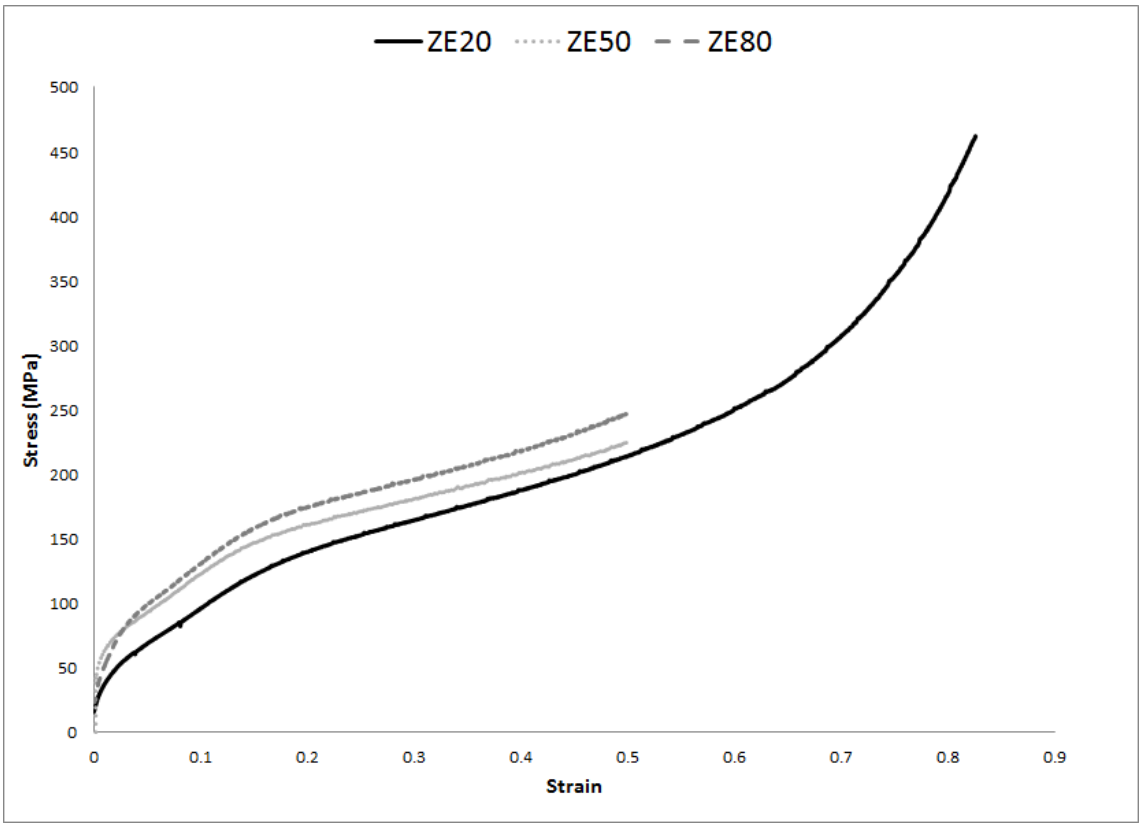

Figure 3: Flow stress-curve obtained for compression of varying zinc contents at a strain rate of 0.01 s^{-1} and temperature of 200°C

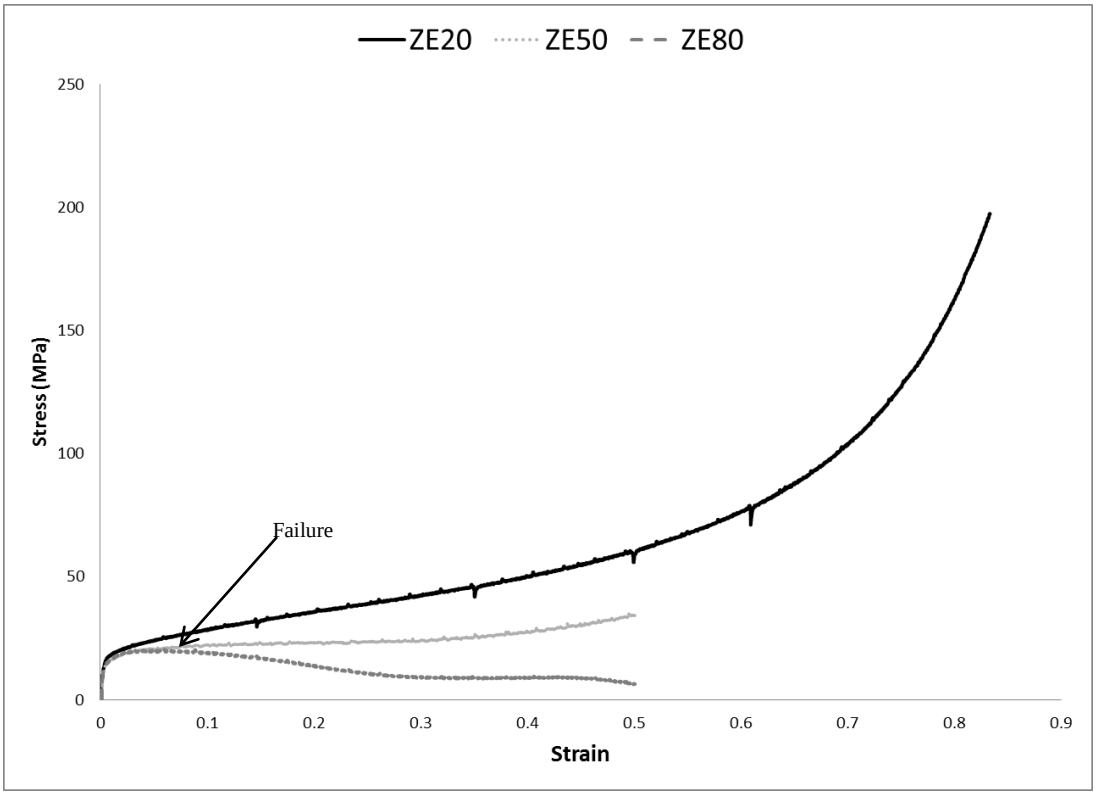

Figure 4: Flow stress-curve obtained for compression of varying zinc contents at a strain rate of 0.01 s^{-1} and temperature of 375°C

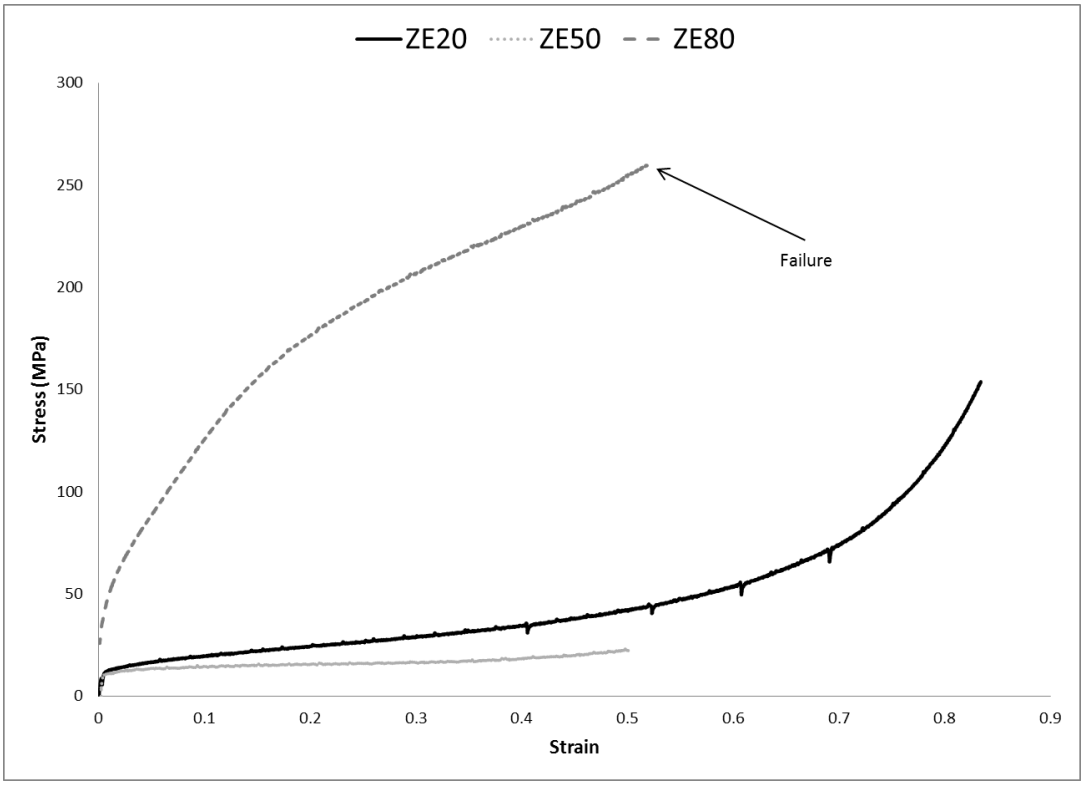

Figure 5: Flow stress-curve obtained for compression of varying zinc contents at a strain rate of 0.01 s^{-1} and temperature of 425°C

The same flow-stress diagrams were constructed for a strain rate of 5/s and can be seen in

Figure 6 through Figure 8

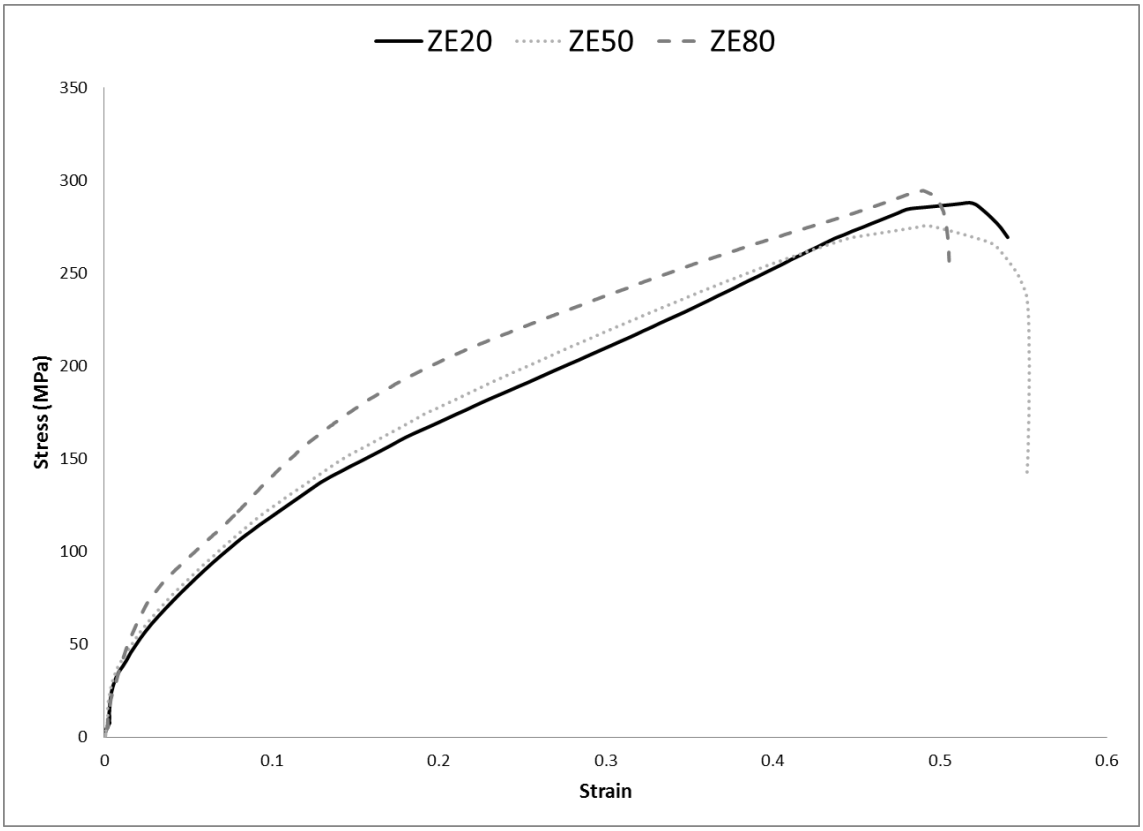

Figure 6: Flow stress-curve obtained for compression of varying zinc contents at a strain rate of 5.0 s^{-1} and temperature of 200°C

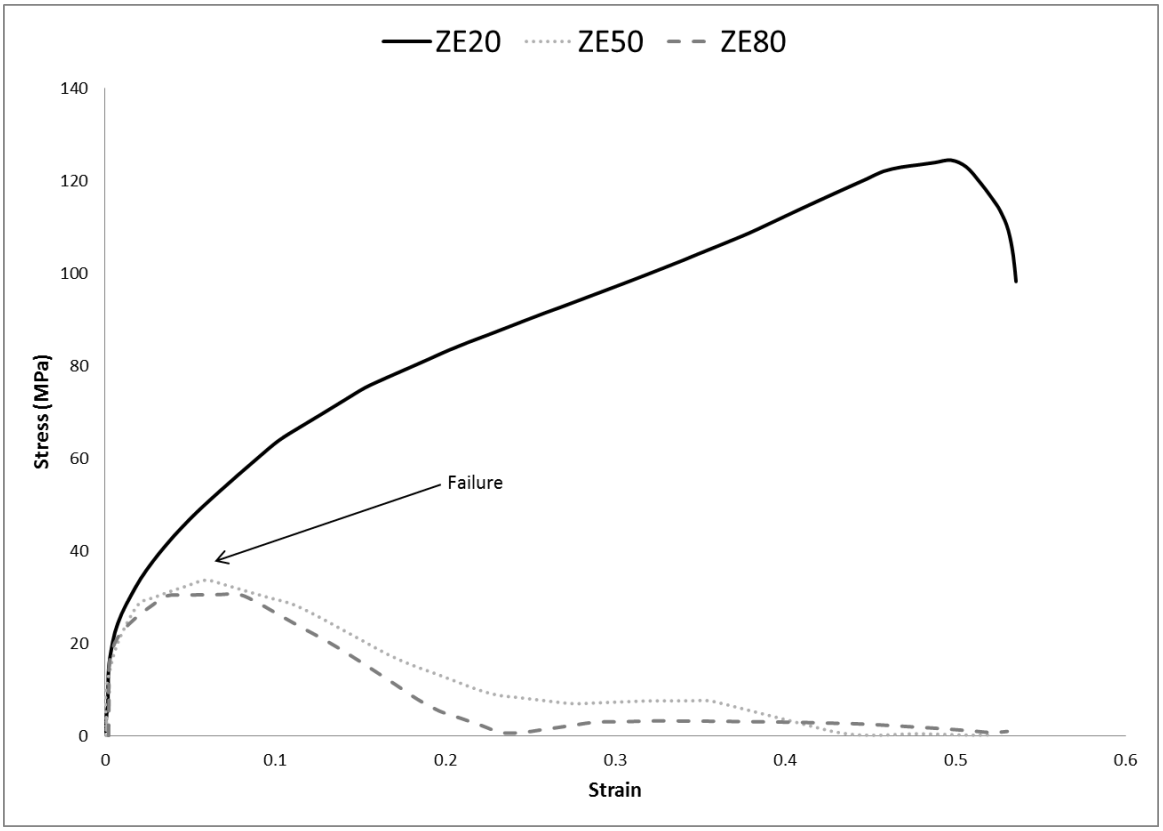

Figure 7: Flow stress-curve obtained for compression of varying zinc contents at a strain rate of 5.0 s-1 and temperature of 375°C

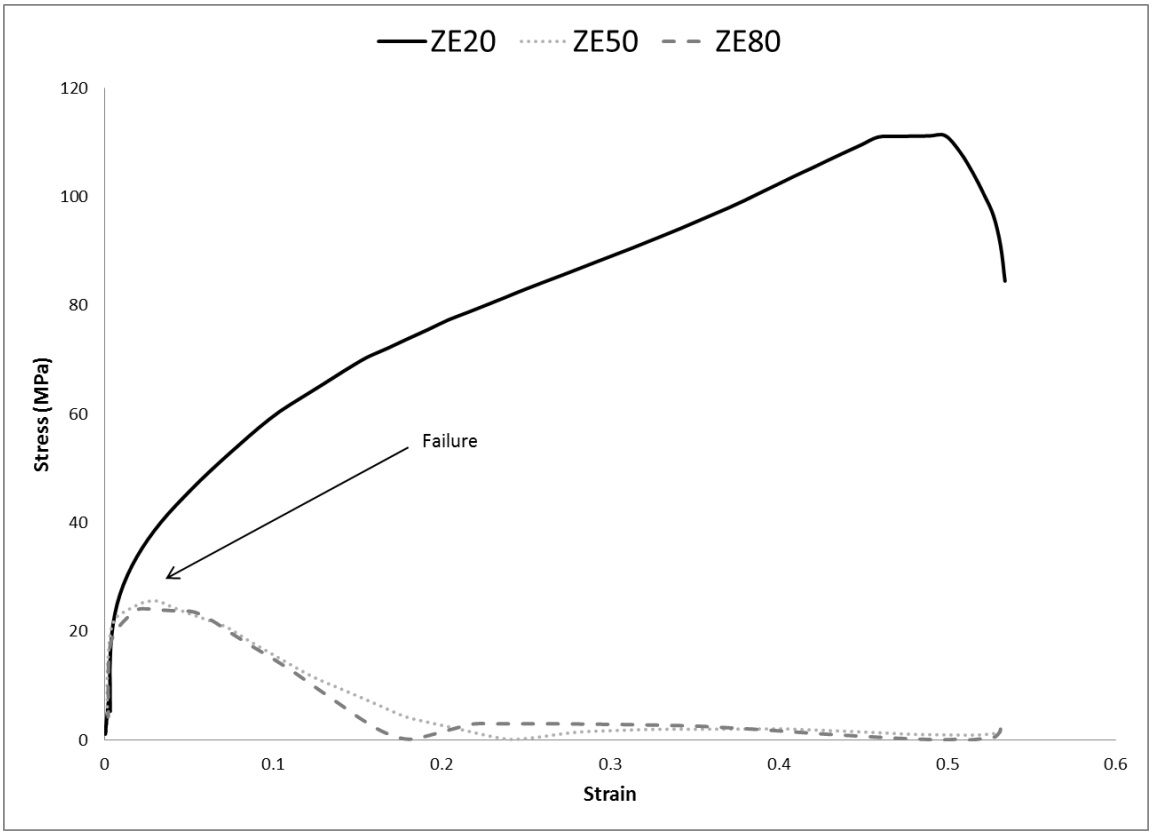

Figure 8: Flow stress-curve obtained for compression of varying zinc contents at a strain rate of 5.0 s-1 and temperature of 425°C

3.3 Metallography Study

A metallographic analysis was conducted in order to observe and better understand underlying morphologies which would be seen in subsequent examinations using electron microscopy. For each of these regions, micrographs focus on the longitudinal direction as this reveals most about the deformation mechanisms enabled. For the scope of this study, the longitudinal direction or cross section refers to micrographs which are looking perpendicular to the compression axis on a plane parallel to the direction of compression. Images aligned in the transverse view or cross section are taken in a perspective looking down the compression axis of each specimen.

A baseline microstructure was established for each alloy through the observation of as-cast metallographic specimens. Observational microscopy was then conducted on

five generalized conditions seen during compression testing: raw condition, low strain rate/low temperature, high strain rate/low temperature, low strain rate/high temperature, and high strain rate/high temperature. The following subsections will present the resulting micrographs according to these conditions.

3.3.1 Raw Material

Raw material specimens were examined in order to establish a baseline grain morphology and texture. Each of the samples were examined at lower magnifications which were sufficient to demonstrate the representative structures. As-cast structures can be seen in Figure 9a through Figure 9c respectively

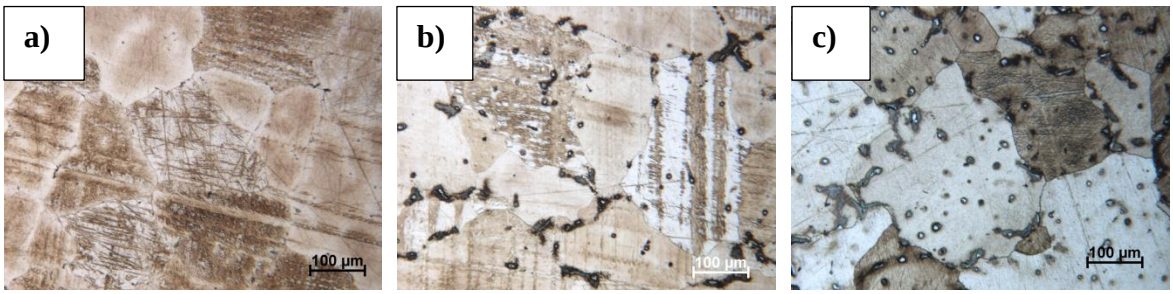

Figure 9: Micrographs obtained via LOM of a) raw ZE20, b) raw ZE50, and c) raw ZE80 etched in diluted picric acid and glacial acetic acid

Each of these micrographs exhibit equiax, coarse grains structure with grains on the order of 100-300 microns. Twinning is evident in some of the micrographs; in underformed, raw material these are thought to be artifacts originating from sectioning and metallographic preparation. Cast micrographs for each alloy system appear to be similar both in grain size and geometry.

3.3.2 Low strain rate, low temperature

Low strain rate, low temperature compressions were conducted at .01/s and 200°C respectively. For each zinc content of ZExx alloy, a micrograph representing the typical

field seen in each alloy in the longitudinal direction for ZE20, ZE50, and ZE80 are shown in Figure 10a through Figure 10c respectively.

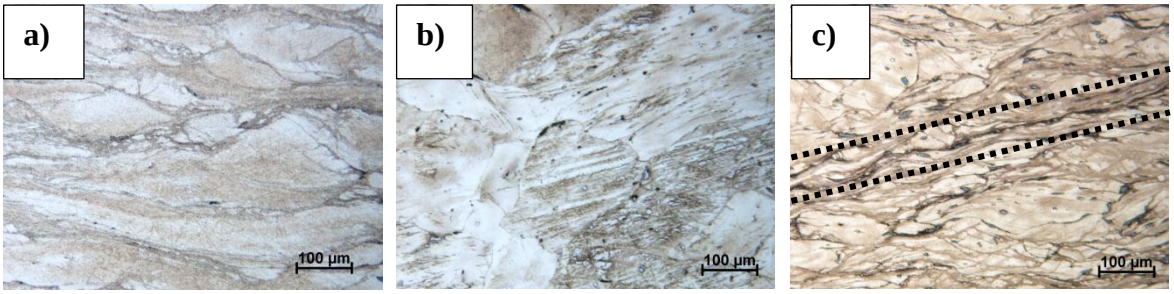

Figure 10: Longitudinal view micrographs obtained via LOM of a) ZE20, b) ZE50, and c) ZE80 deformed at a strain rate of 0.01 s^1 and a temperature of 200°C etched in diluted picric acid and glacial acetic acid

It is important to note that for the preceding micrographs, ZE20 and ZE80 in Figure 10a and Figure 10c were deformed to a strain of 0.8 while ZE50 was only deformed to a strain of 0.5. Because of these differences in strain, the physical appearance of the ZE50 is much less deformed with grains with a lower aspect ratio since the specimen had not been compressed as much.

In general, each of these micrographs show deformed grains with grain flattening relative to the compression direction. As an estimation grain size in the direction orthogonal to the compression direction can be as high as 500 microns while compression axis dimensions are much lower and even as small as 10 microns. It is also interesting to note that in Figure 10c, ZE80 exhibits a deviation indicating heavy grain sliding leading into fracture marked between the dotted lines.

3.3.3 High strain rate, low temperature

Longitudinal light optical micrographs in the for compression samples compressed at a strain rate of 5/s and 200°C can be seen in Figure 11a and Figure 11b.

For these compression parameters, only ZE20 and ZE50 were run without complete disintegration, therefore there is no micrograph for ZE80.

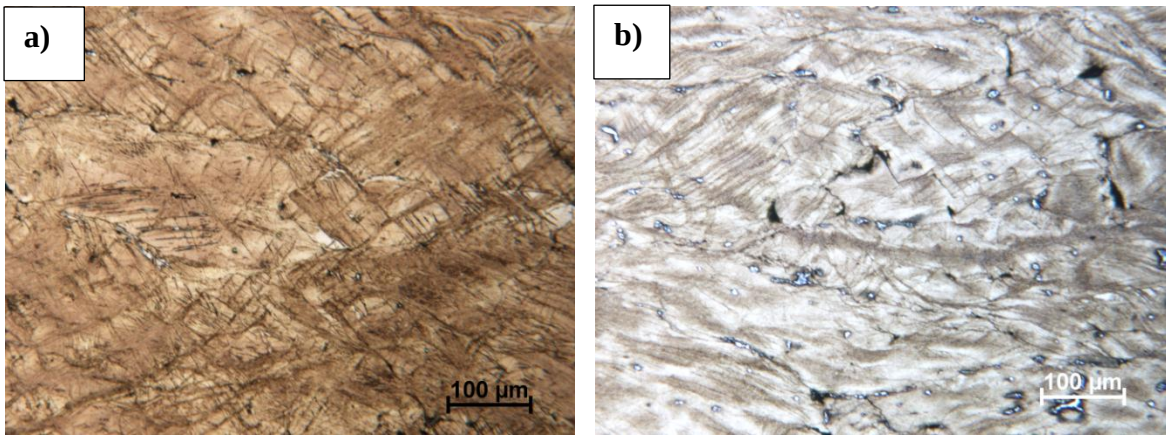

Figure 11: Longitudinal view micrographs obtained via LOM of a) ZE20 and b) ZE50 deformed at a strain rate of 5.0 s^{-1} and a temperature of 200°C etched in diluted picric acid and glacial acetic acid

These micrographs show a large degree of grain deformation while retaining sizes relative to the starting grain size seen in the as-cast material. The grain aspect ratio is such that grain dimensions were compressed along the compression axis and elongated in the radial direction which is orthogonal to the compression axis. In each micrograph, a heavy degree of twinning within grain boundaries is visible. Each micrograph exhibits a small degree of pitting and voiding at the grain boundaries which are artifact features due to corrosion during metallographic preparation.

In order to verify grain structure and to further examine for the presence of fine grain structure, these compression samples were examined in the transverse direction seen in Figure 12a and Figure **12**b.

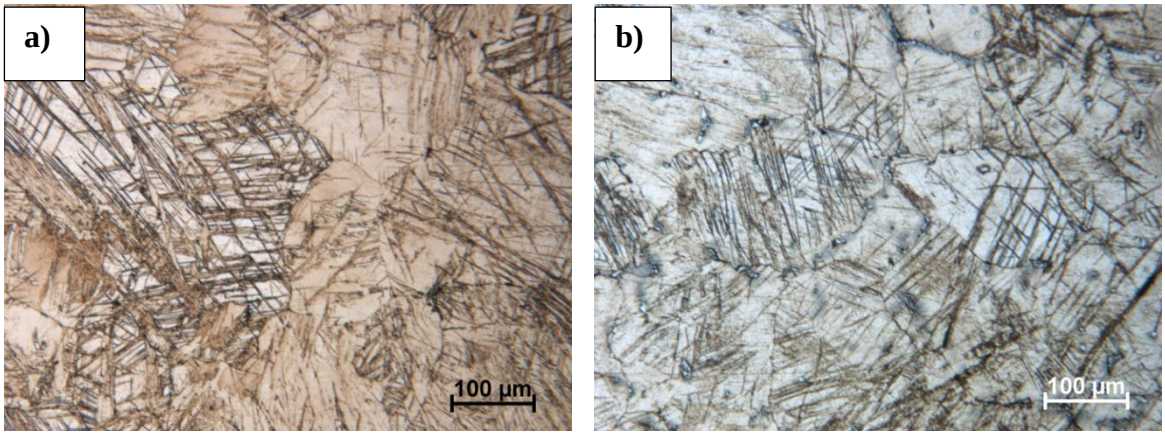

Figure 12: Transverse view micrographs obtained via LOM of a) ZE20 and b) ZE50 deformed at a strain rate of 5.0 s-1 and a temperature of 200°C etched in diluted picric acid and glacial acetic acid

Each field in Figure 12 confirms the coarse-grained nature of each specimen and shows the same heavy degree of twinning. In these fields, grain deformation is not visible due to the perspective relative to the compression axis.

3.3.4 Low strain rate, high temperature

For the low strain (0.01/s), high temperature (425°C) condition, representative micrographs in the longitudinal direction of ZE20 and ZE50 can be seen in Figure 13. This condition does not feature a ZE80 micrograph since the specimen failed catastrophically and hence cannot be metallographically examined.

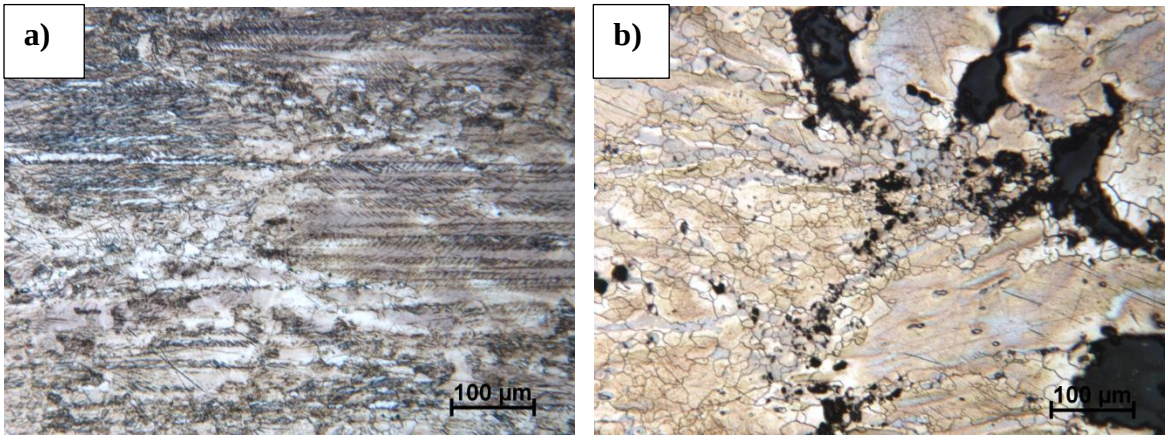

Figure 13: Longitudinal view micrographs obtained via LOM of a) ZE20 and b) ZE50 deformed at a strain rate of 0.01 s-1 and a temperature of 425°C etched in diluted picric acid and glacial acetic acid

Each compression specimen in this condition feature a duplex grain structure both with very coarse grains on the order of 500 microns with fine grains ranging from 5-15 microns. It is also interesting to note that in the case of ZE50 in Figure 13b the sample began to fail which can be seen by the dark regions in the image which are voids resulting from compression trials.

A higher magnification image of the fine grained structure in ZE20 can be seen in Figure 14

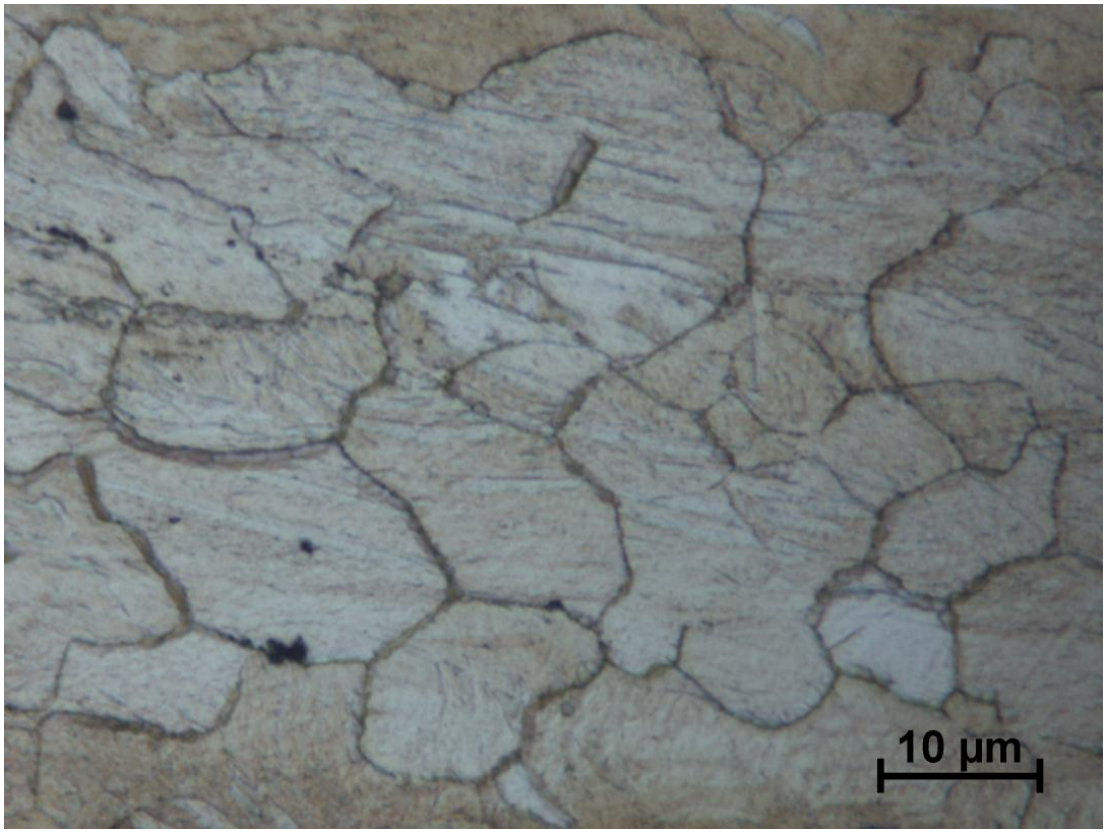

Figure 14: Optical micrograph of fine-grained region seen in the longitudinal orientation of ZE 20 deformed at a strain rate of 0.01 s-1 and a temperature of 425°C etched in diluted picric acid and glacial acetic acid

This micrograph shows very fine grains which measure as small as 5 microns and as large as 15 microns. Typically these regions were seen in a pattern and bound by coarse grains as shown in Figure 15

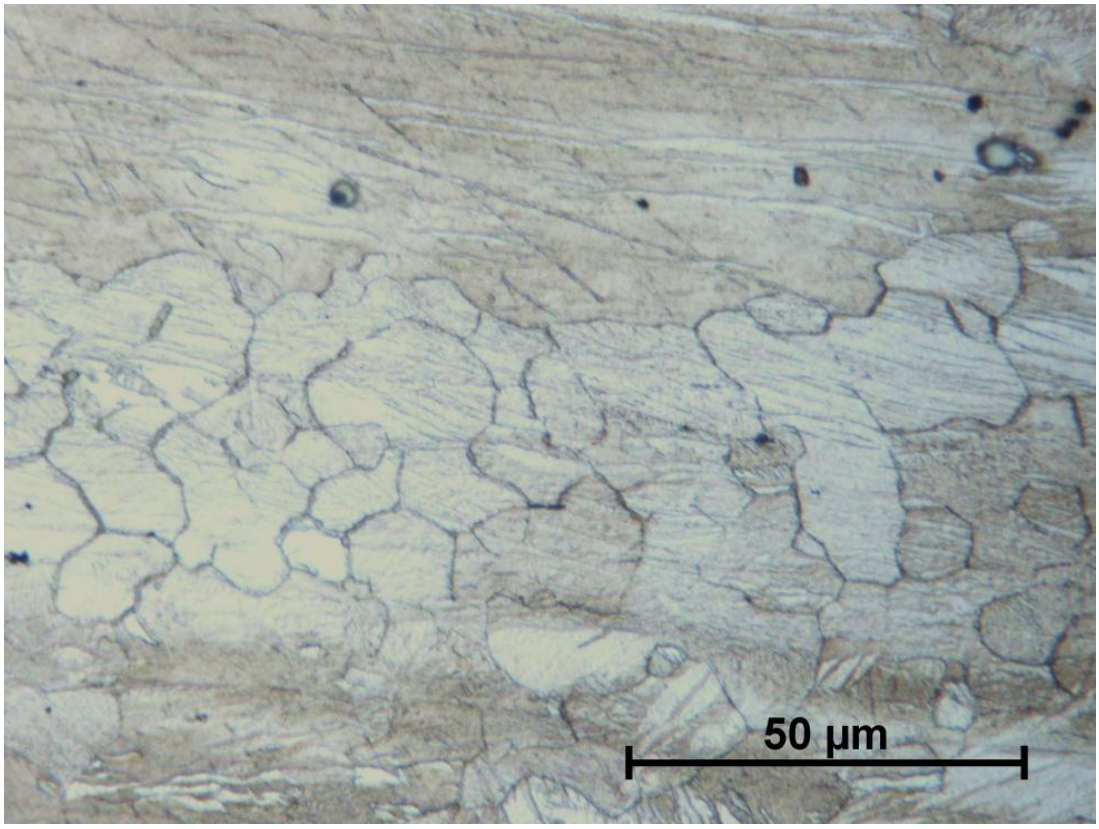

Figure 15: Optical micrograph of typical duplex structure seen in ZE20 deformed at a strain rate of 0.01 s-1 and a temperature of 425°C etched in diluted picric acid and glacial acetic acid

Twinning is present in both the fine grain and the coarse grain regions however is seen to be more pronounced within coarse grains.

A similar duplex structure with comparable coarse grain size was seen in the ZE50 system compressed at these conditions. A micrograph showing a higher magnification image of this duplex region can be seen in Figure 16

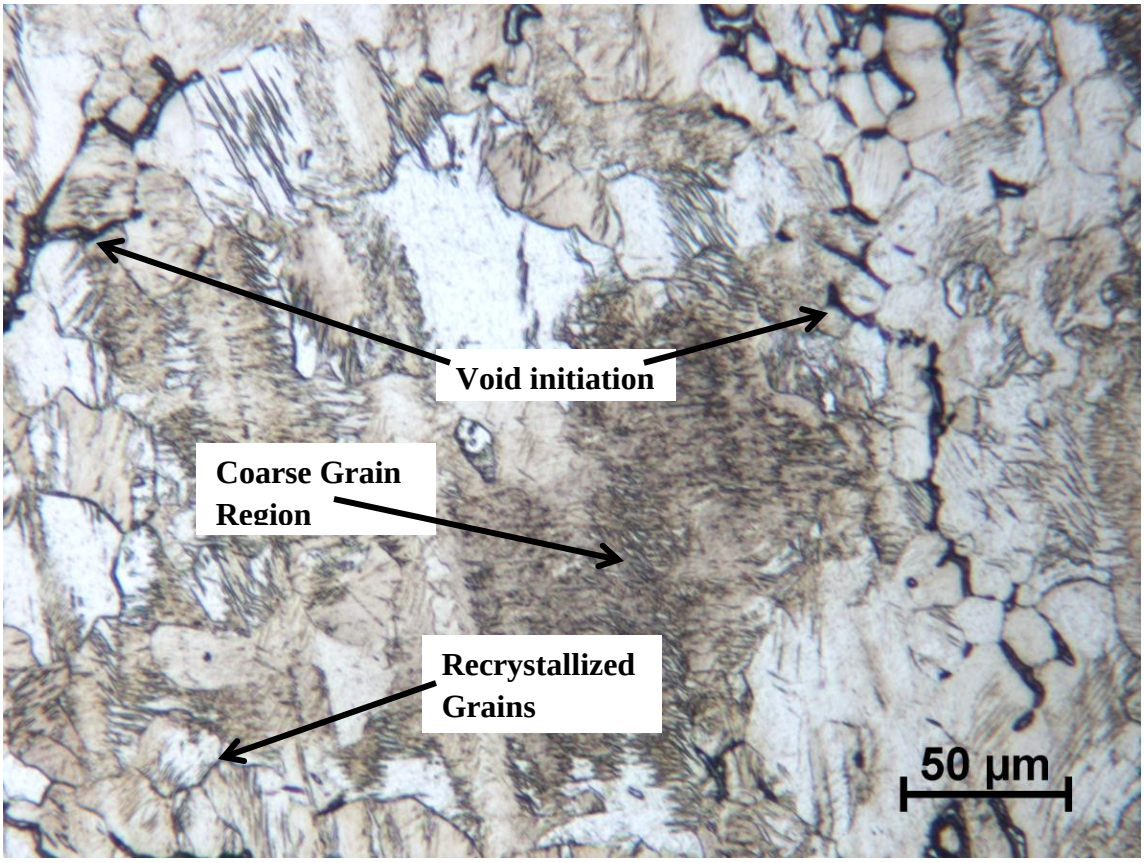

Figure 16: Optical micrograph of typical duplex structure seen in ZE50 deformed at a strain rate of 0.01 s-1 and a temperature of 425°C etched in diluted picric acid and glacial acetic acid

Figure 16 also shows the initiation of failure in the fine grain region, seen as a pronounced, dark boundary on the right side of the micrograph. Typically the fine grained regions in ZE50 were seen to reside at void initiation sites with failure taking place around grain boundaries as evidenced by Figure 17.

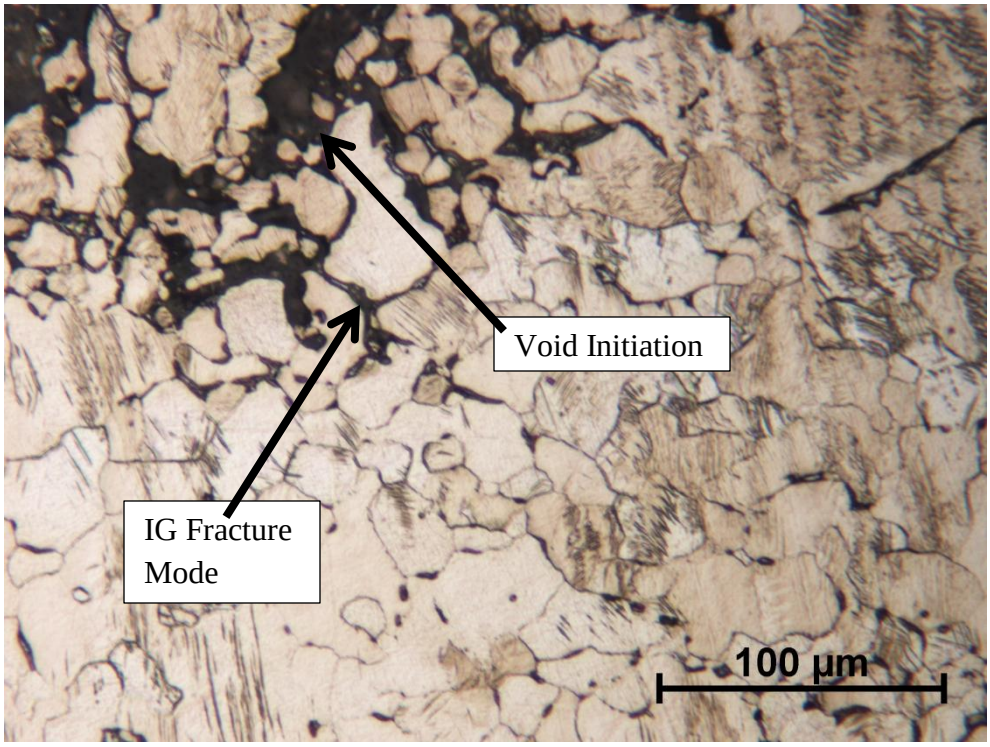

Figure 17: Intergranular fracture visible in optical micrograph of a ZE50 deformed at a strain rate of 0.01 s-1 and a temperature of 425°C

Voiding in this figure is seen as the dark region seen in the top left of the image. In comparison the ZE20 alloy, ZE50 fine-grains had a slightly different morphology shown in Figure 18.

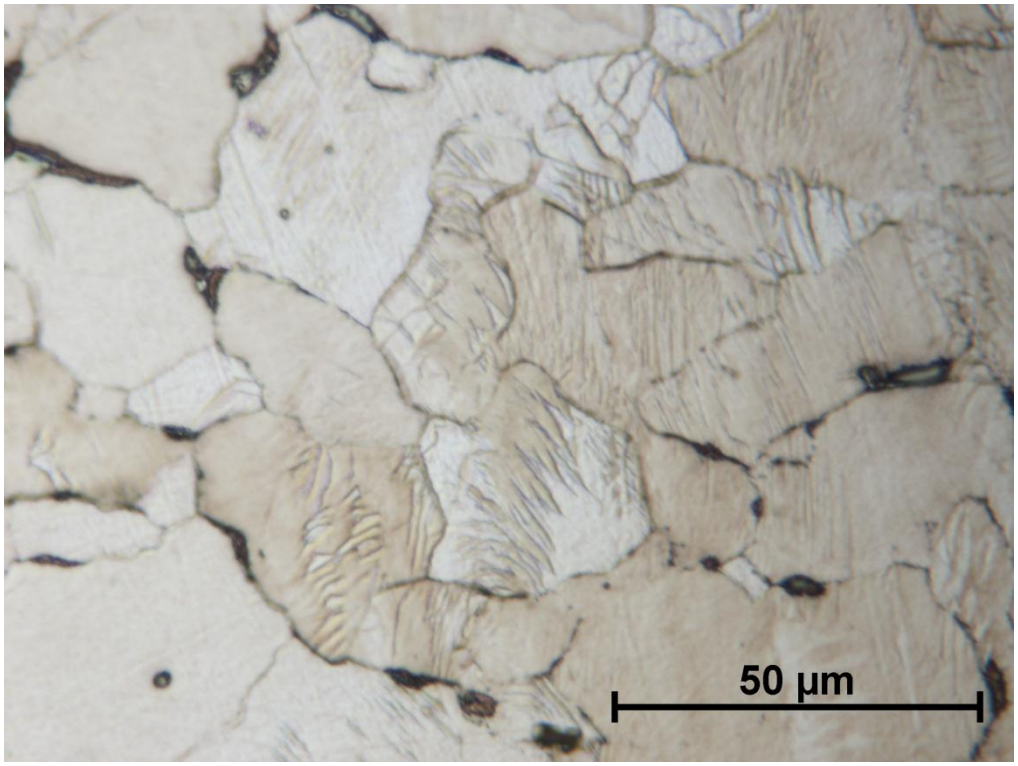

Figure 18: Optical micrograph of fine-grained region seen in the longitudinal orientation of ZE50 deformed at a strain rate of 0.01 s-1 and a temperature of 425°C etched in diluted picric acid and glacial acetic acid

In general, the ZE50 fine grain region had grains as large as 50 microns, exhibited a slightly deformed structure and even exhibited some twinning within grains. The deformation in this figure occurred vertical relative to the micrograph. This is seen as the shape of the grains is compressed in the vertical direction.

3.3.5 High strain rate, high temperature

At a strain rate of 5/s and temperature of 425°C, ZE20 was the only alloy which was able to be successfully be compressed without failure. A light optical micrograph in the longitudinal direction of ZE20 compressed at these conditions can be seen in Figure 19.

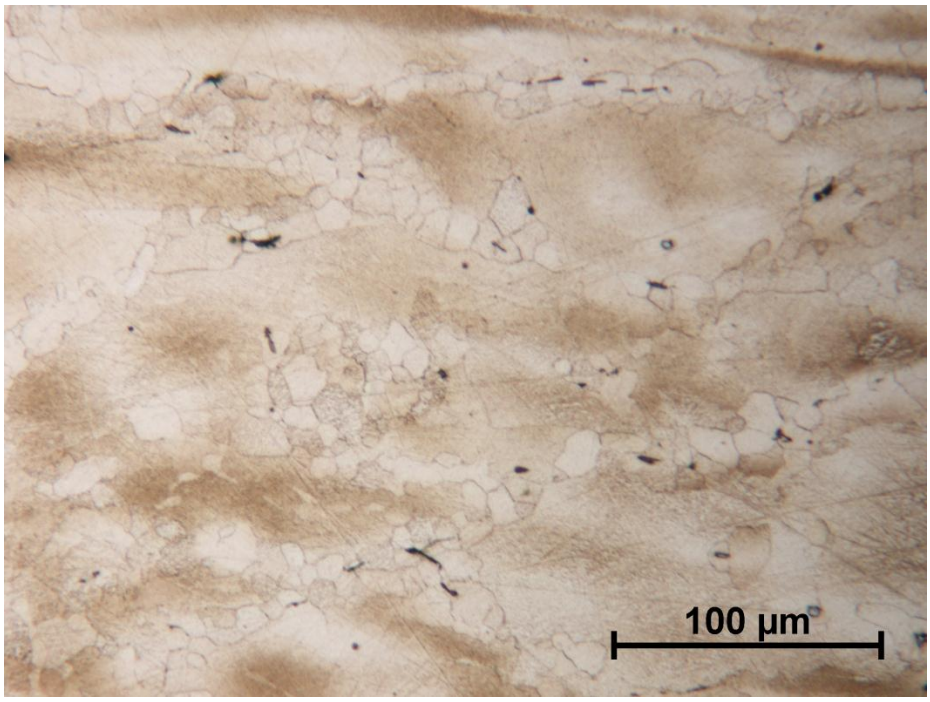

Figure 19: Optical micrograph representing typical field oriented longitudinally seen in ZE20 deformed at a strain rate of 5.0 s-1 and a temperature of 425°C etched in diluted picric acid and glacial acetic acid

This micrograph shows a duplex grain structure with fine grains tending to exist in clusters along coarse grain boundaries. Coarse grains in this condition did not exhibit as severe of an aspect ratio as other compressed microstructures. To classify fine grain size a high magnification image of a refined zone was obtained and can be seen in Figure 20.

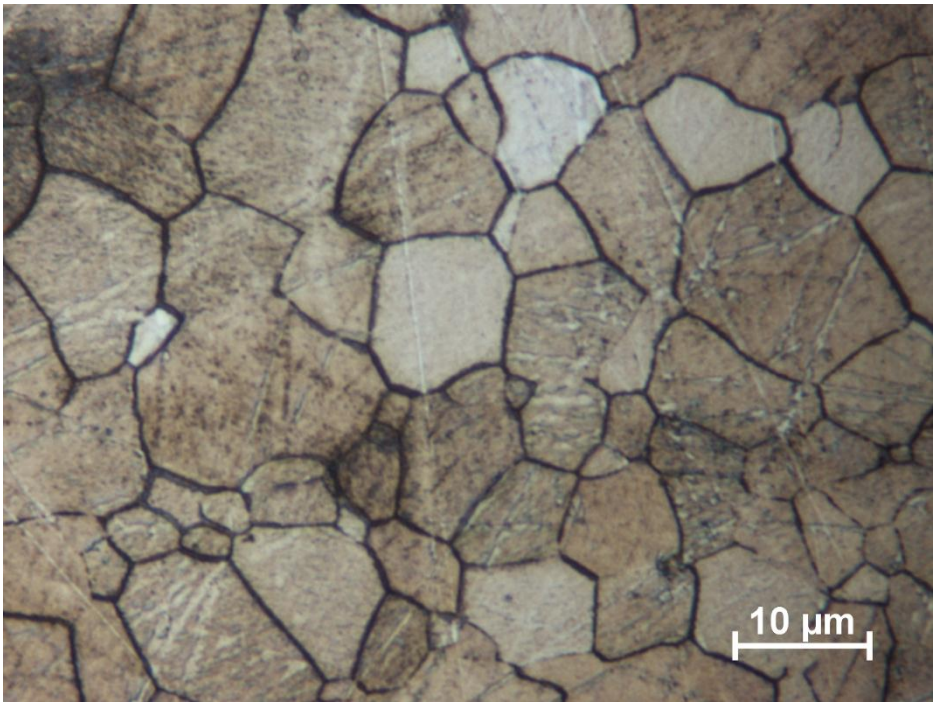

Figure 20: Optical micrograph showing refined grain region typically seen in longitudinal direction of ZE20 deformed at a strain rate of 5.0 s-1 and a temperature of 425°C etched in diluted picric acid and glacial acetic acid

This refined zone shows grains ranging from 1 micron to 15 microns in diameter. Additionally, twinning within grain areas is minimal compared to fields seen in other compression samples.

A transverse orientation of this structure was examined and a representative general field can be seen in Figure 21.

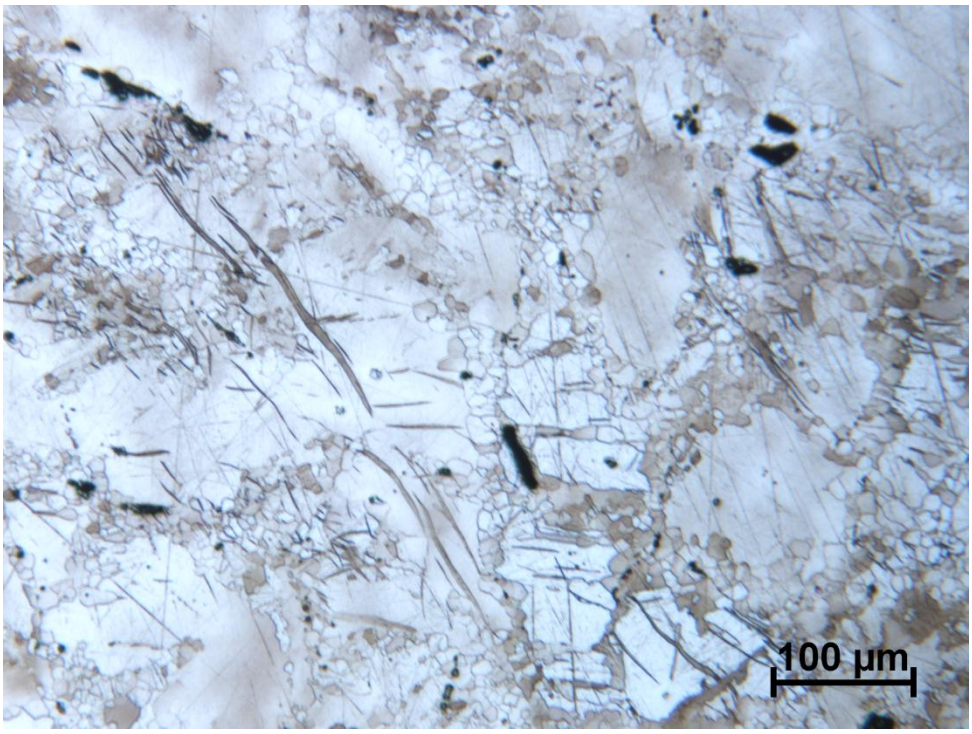

Figure 21: Transverse orientation micrograph of ZE20 deformed at a strain rate of 5.0 s-1 and a temperature of 425°C etched in diluted picric acid and glacial acetic acid representing general grain morphology

It is interesting to note that nearly the same morphology is seen as in Figure 19 with the exception of a higher degree of twins within coarse grains. Some coarse grain regions in this view appear to be large continuous zones bounded by fine-grained clusters. A refined grain region was also examined in the transverse view and can be seen in Figure 22.

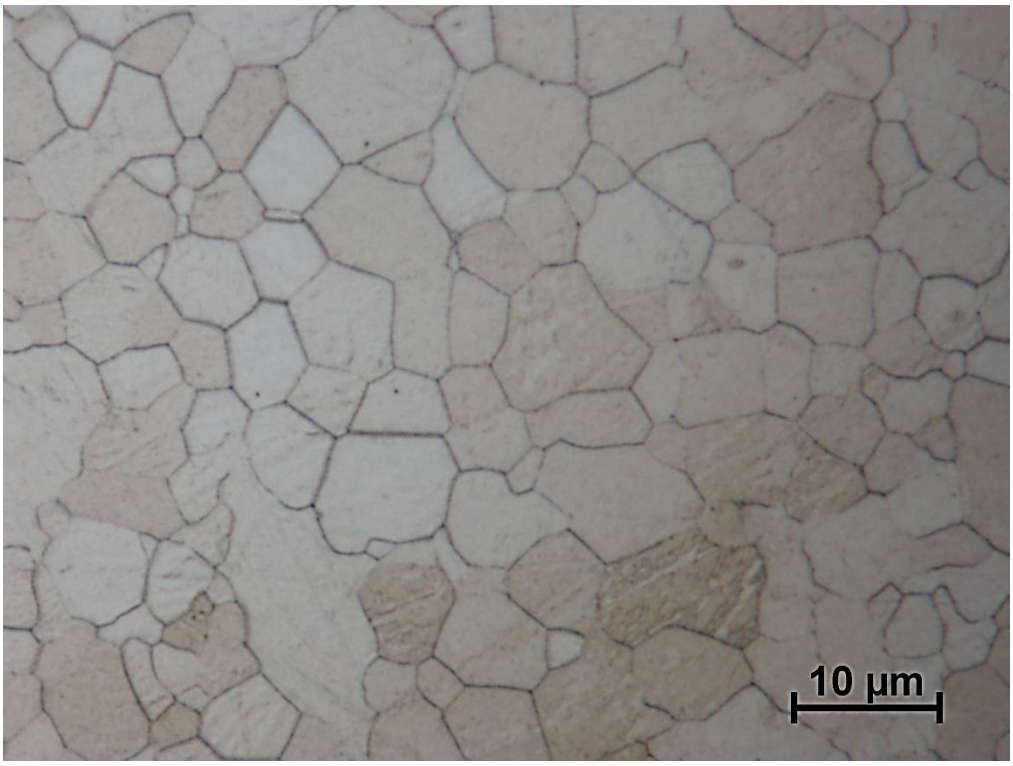

Figure 22: Transverse orientation micrograph of ZE20 deformed at a strain rate of 5.0 s-1 and a temperature of 425°C etched in diluted picric acid and glacial acetic acid representing refined grain region

The morphology in this field is identical to that seen in the longitudinal view in Figure 20.

3.4 SEM Results

3.4.1 Mode II failure classification via SEM micrographs

A sample that fractured via mode II as seen in Figure 2c was examined via SEM to conduct a fractography study. Several images of the fracture surface were obtained exhibiting the most unique features seen associated with this failure mode. A representation of a general field can be seen in Figure 23.

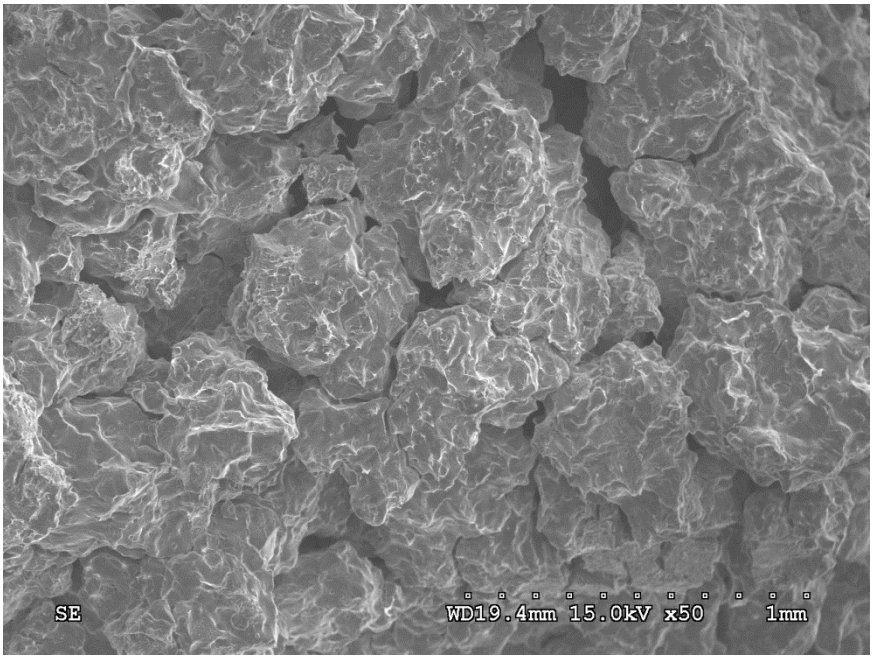

Figure 23: SEM micrograph of mode II fracture surface showing intergranular-type failure characteristic

In this field, it is possible to distinguish what appear to be individual, separated grains indicating a possible intergranular fracture mechanism.

Higher magnification examinations of this surface that can be used to explain the mechanics of failure during compression and will be show in in subsequent figures. At magnifications of 500X ductile features were observed as seen in Figure 24.

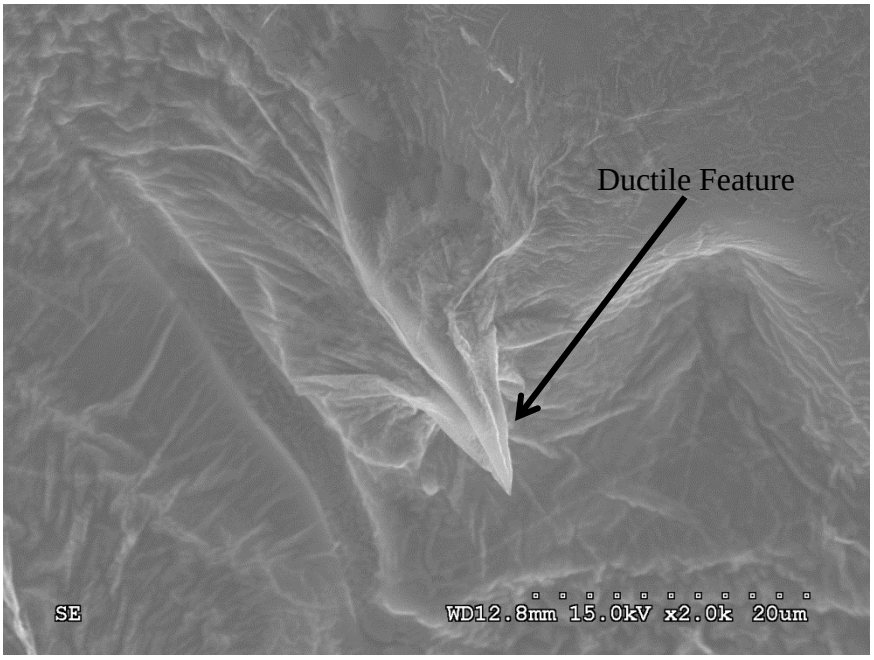

Figure 24: Electron micrograph showing ductile feature on the fracture surface oriented radially relative to the compression axis

High magnification SEM micrographs also revealed a surface with a non-uniform topography and can be seen in Figure 25.

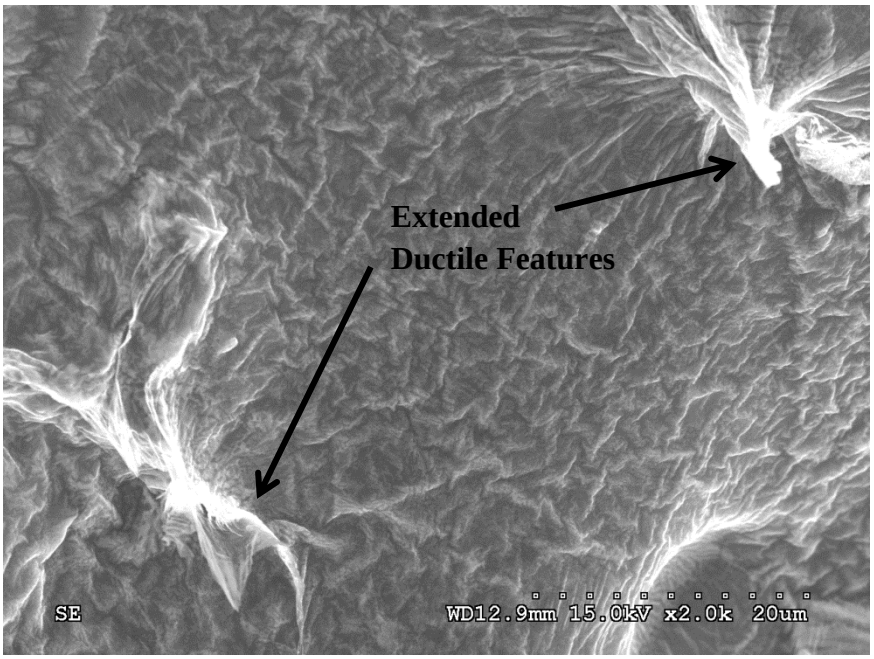

Figure 25: Electron micrograph showing typical surface topography seen on fracture surfaces in mode II failure

SEM micrographs were also taken of a ZE50 specimen which had begun to show signs of intergranular (IG) failure but failed in mode I during compression testing. This micrograph can be seen in Figure 26. Note that this image shows intermetallics that lay along crack roots.

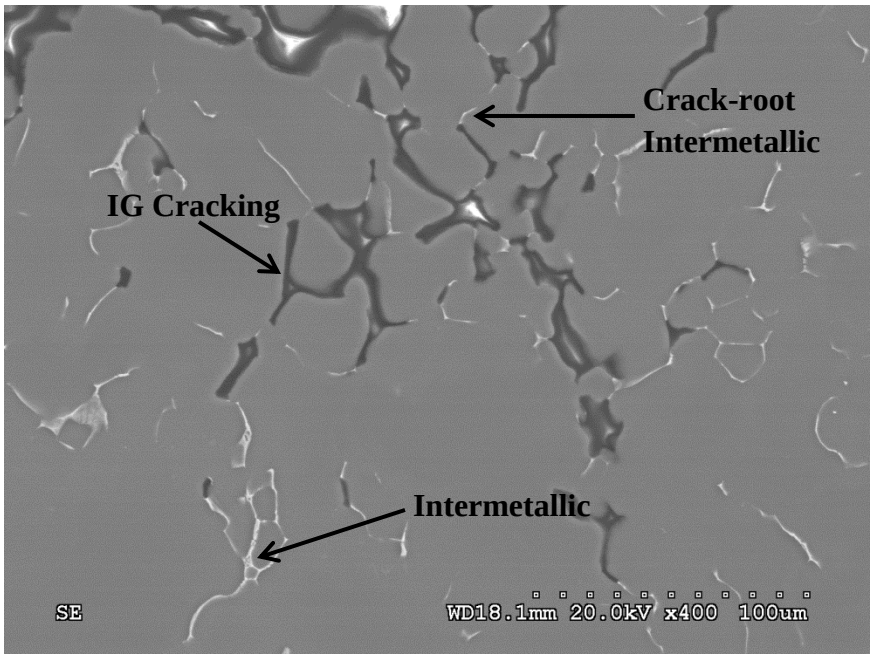

Figure 26: Initiation site of failure with voids growing at grain boundaries showing high incidence of intermetallic at crack roots

These crack regions can be discerned to not be artifacts of metallographic preparation due to their relatively large width of 5 to 10 microns.

3.4.2 Phase classification via SEM micrographs and EDS mapping

A large amount of a eutectic constituent was observed in all fields studied and a representative micrograph of this morphology can be seen in Figure 27.

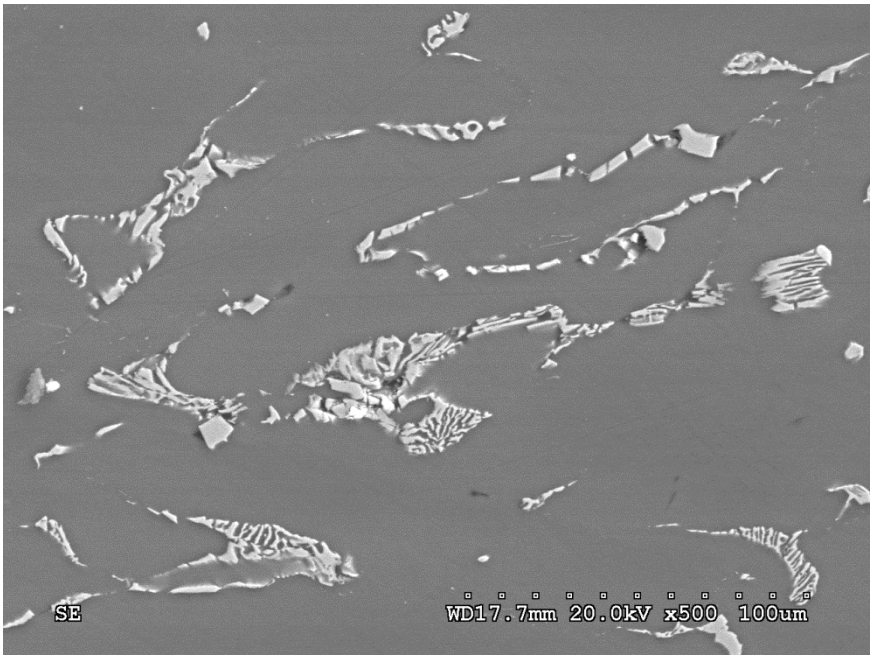

Figure 27: Lamellar phase structure observed via SEM analysis used as region of interest (ROI) for EDS mapping

This structure was determined to be a eutectic compound based on the lamellar structure seen in the image. The darker phase is the magnesium matrix while the lighter constituent is believed to be a Mg-Zn compound, based on relative Zn content in the alloy.

Energy dispersive spectroscopy (EDS) was conducted on several regions of interest where there were higher amount of precipitate and intermetallic phases. Upon initial examination of the SEM micrographs, it was seen that there were two distinctive morphologies: one which was more curved in nature and frequently exhibited a lamellar structure as seen in Figure 27, and another which consisted of straight, blocky stringers as seen in Figure 28.

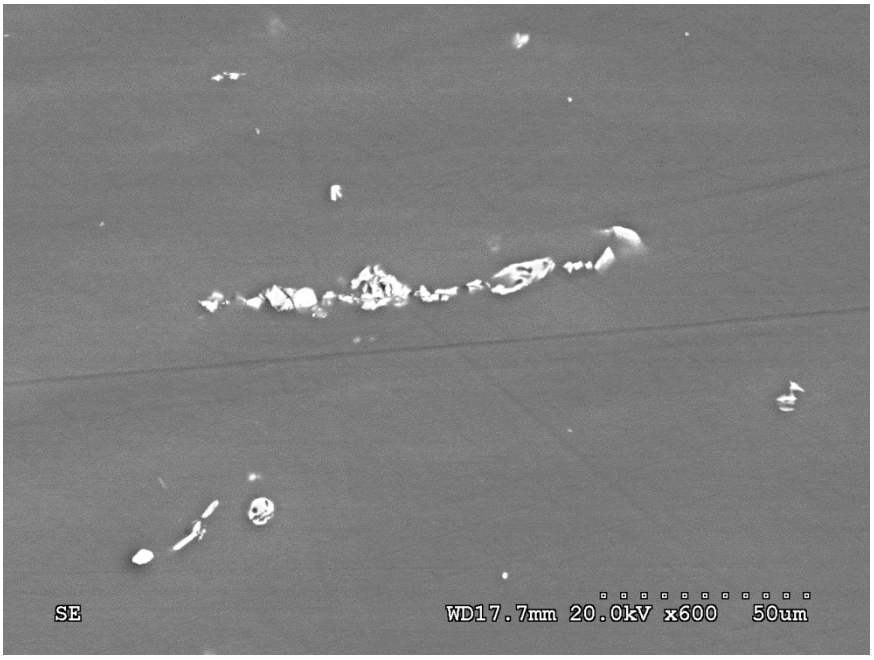

Figure 28: Blocky, stringer phase observed via SEM analysis used as region of interest (ROI) for EDS mapping (compression direction perpendicular to field of view)

An EDS map was collected in order to determine the relative chemistries of the field of view and classify the phase morphology in each view. EDS maps output color heat maps which should intense colors in regions of high element instance. By creating these maps, individual constituent-rich regions can be resolved in order to determine phase layout. First, the curve constituent seen in most fields was examined. The corresponding EDS maps to Figure 27 can be seen in Figure 29a through Figure 29c representing magnesium, zinc, and cerium respectively.

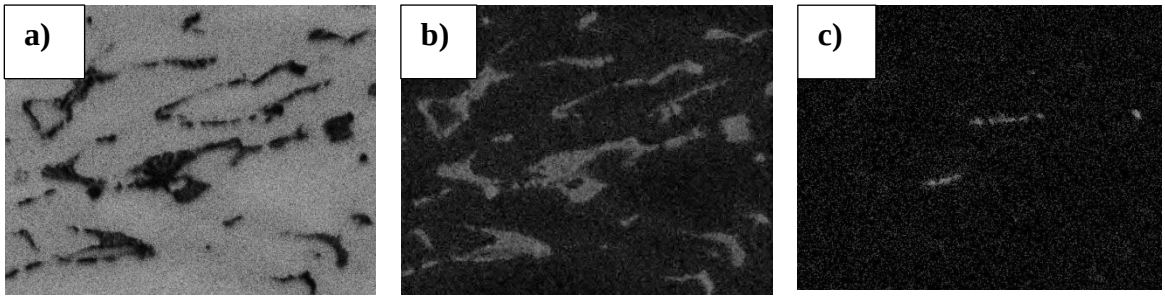

Figure 29: EDS maps corresponding to ROI of curved lamellar structure showing element maps for a) Magnesium, b) Zinc, and c) Cerium

The blocky intermetallic in Figure 28 was examined using the same EDS mapping technique. A corresponding EDS map corresponding can be seen for magnesium, zinc and cerium in Figure 30a through c respectively.

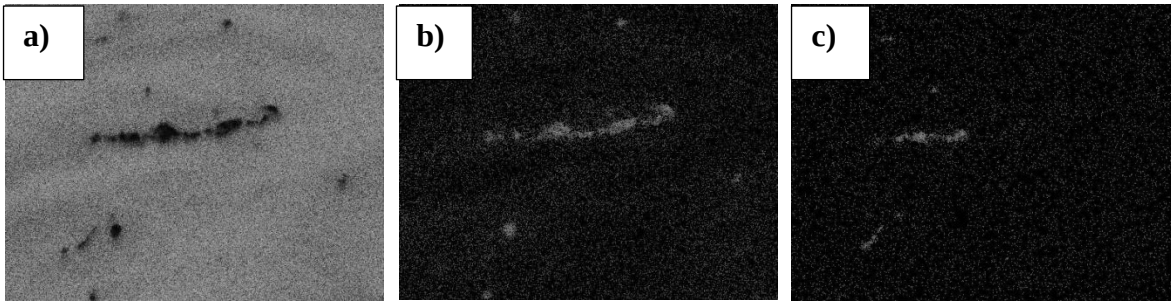

Figure 30: EDS maps corresponding to ROI of blocky structure showing element maps for a) Magnesium, b) Zinc, and c) Cerium

These micrographs demonstrate that this constituent is composed of both a Mg-Zn and Mg-Ce binary, however appear very difficult to resolve from one another.

During EDS mapping, grain boundary chemistry inhomogeneitys were observed. To optimize display of this feature, an EDS map was collected for 0.5 hours while operating the microscope in a high-current configuration. The secondary electron image as well as EDS maps of Mg and Zn can be seen in Figure 31.

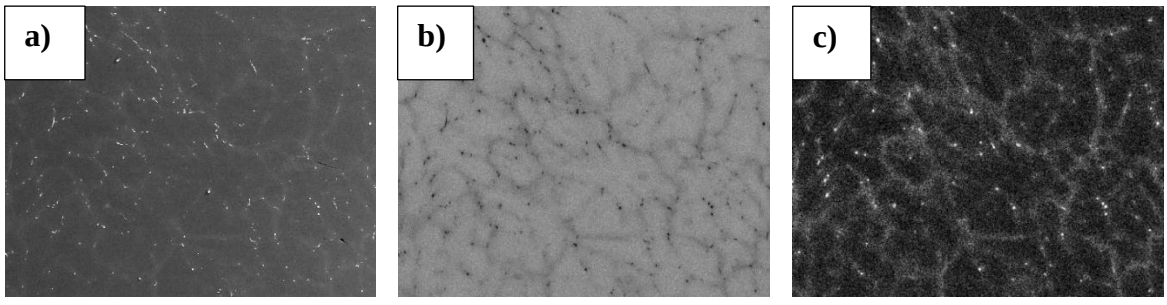

Figure 31: EDS map showing inhomogeneous chemistry at grain boundaries depicting a) Electron micrograph obtained using secondary elections, b) Magnesium EDS map, and c) Zinc EDS map

These images shows that there is Mg depletion at the grain boundaries, evidenced by the darker regions of the EDS map. Furthermore, the zinc map in Figure 31c highlights zinc content through bright regions and suggests a zinc migration to the grain boundaries.

3.4.3 Grain orientation mapping via electron back-scatter diffraction (EBSD)

Grain orientation maps were acquired from various compression samples using EDAX OIM acquisition and OIM analysis software. These maps were collected in order to classify the grain texture before and after deformation in order to establish a transition, if any, from basal to non-basal type grain texture. Areas of interest were selected where the patterns that generated high confidence indexes could be found. The confidence index refers to the degree of fit between the diffraction patterns stored in the computer database, and those that are observed from the sample.

In order to establish a baseline texture, orientation maps were collected from metallographic specimens of as-cast material. These maps are represented in inverse pole-figure maps (IPF) which represent the crystallographic orientation relative to the incident beam. The color on these maps corresponds the accompanying color legends; if a grain appears as a shade of red, and red is closest to the <0001> on the legend, then the grain is aligned in the or near the <0001> direction. It is important to note that often times a significant amount of noise is visible in these patterns manifesting as random blocks of color. This noise can be attributed to the uneven specimen topography or poor surface quality which interferes with the incident beam

IPF maps representing the as cast alloys can be seen below; Figure 32a through Figure 32c represent alloys ZE20, ZE50, and ZE80 respectively.

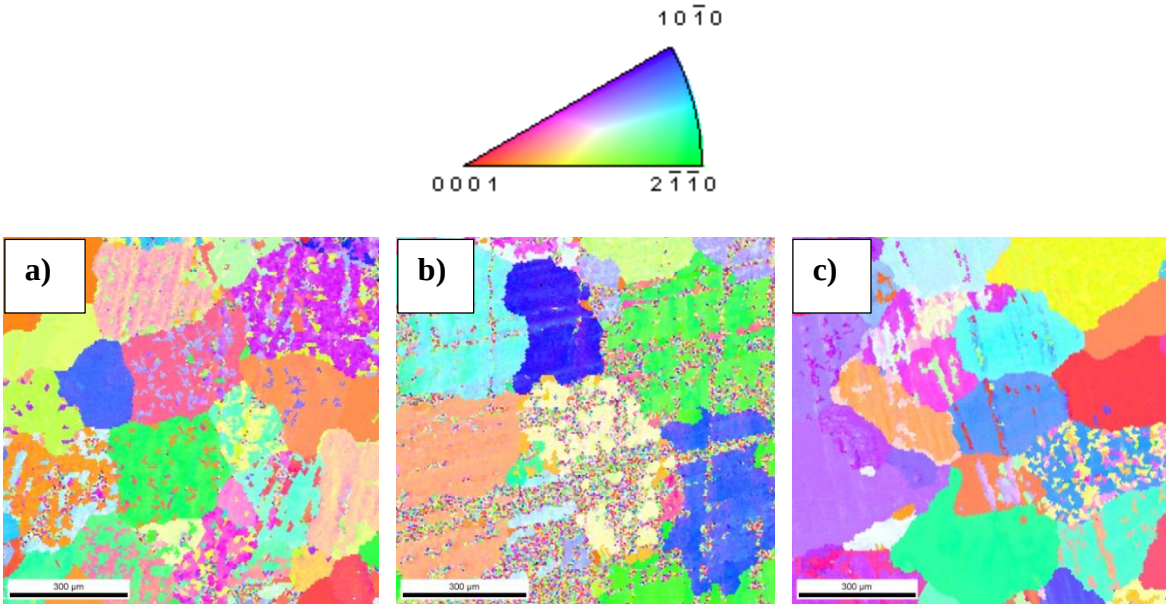

Figure 32: Inverse pole figure (IPF) maps for as cast structure of a) ZE20, b) ZE50, and c) ZE80 with accompanying legend

These maps depict a grain structure which is fairly randomized indicating that the starting grain texture is non-basal. In order to ensure that machining of the compression bars did not induce any changes of texture, an EBSD pattern was created of a machined ZE80 bar, its IPF can be seen in Figure 33

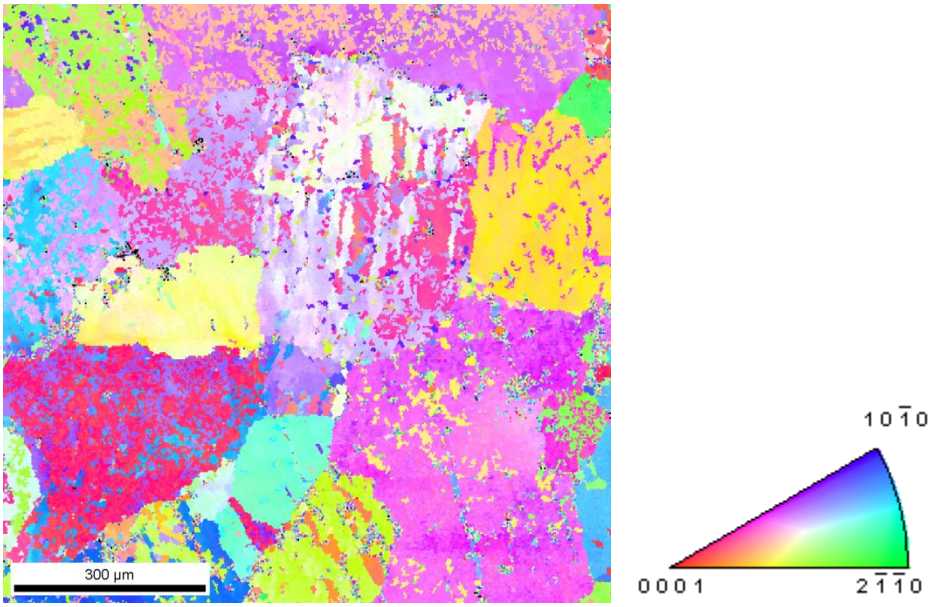

Figure 33: IPF map showing EBSD for ZE80 compression bar perpendicular to long dimension

Like the raw samples, grain texture in the machined compression bar was also randomized indicating that the energy input by the machining process did not cause any grain alignment or recrystallization.

IPFs of deformed specimens were then obtained to examine the effects of deformation on each sample. A representative field of compression samples which did not show refined grain regions for each alloy can be seen in Figure 34.

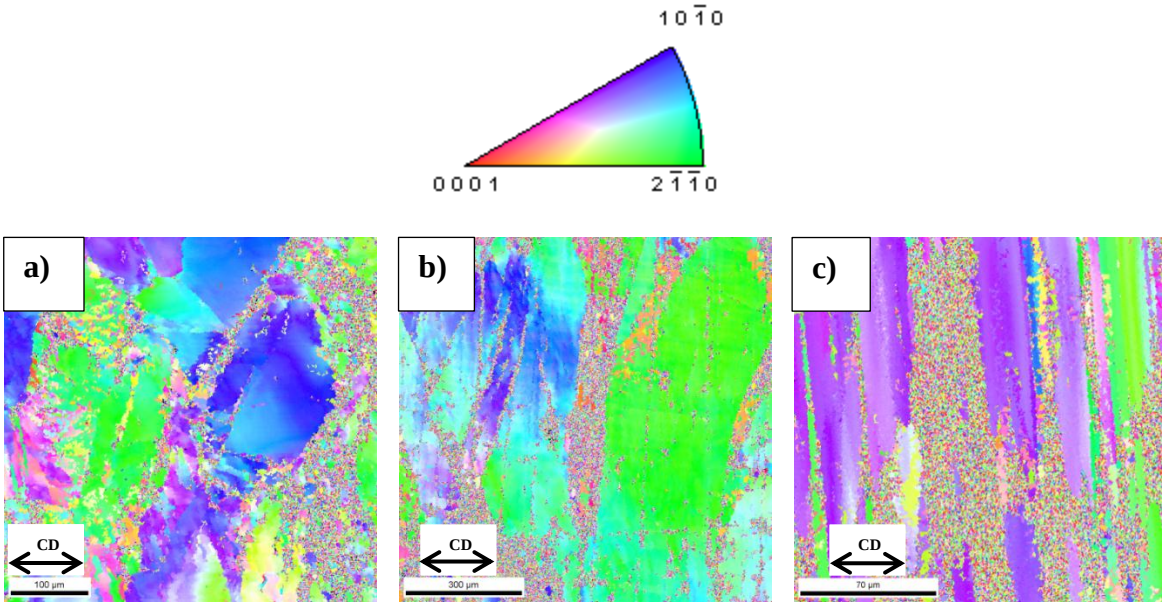

Figure 34: IPF maps showing crystal orientation in the longitudinal direction (compression direction = CD) of samples deformed at 200°C and a strain rate of 0.01/s for a) ZE20, b) ZE50, and c) ZE80

These figures show a high degree of alignment evidenced by closely corresponding colors in each of the grain regions. It is important to note that the scale in each image is different; magnifications were selected where discernible patterns could be resolved. The fine, multicolor regions in these IPFs represent noise from the scattering of the incident beam likely due to topography inconsistencies in the compression samples. Each IPF was collected with the compression axis traversing the orientation map aligned horizontally further evidenced by the grain aspect ratio. These maps represent aligned crystallographic directions shown through color correspondence with the IPF legend. Observing ZE50 in Figure 34b, multiple orientations can be seen within a single grain shown by the green and blue color with no definitive grain boundary. This feature is thought to be a twin grain which exhibits local lattice misorientation within one grain.

A sample displaying refined grain structure that was compressed at a strain rate of 5/s and temperature 425°C can be seen in the longitudinal and transverse directions in Figure 35a and b respectively.

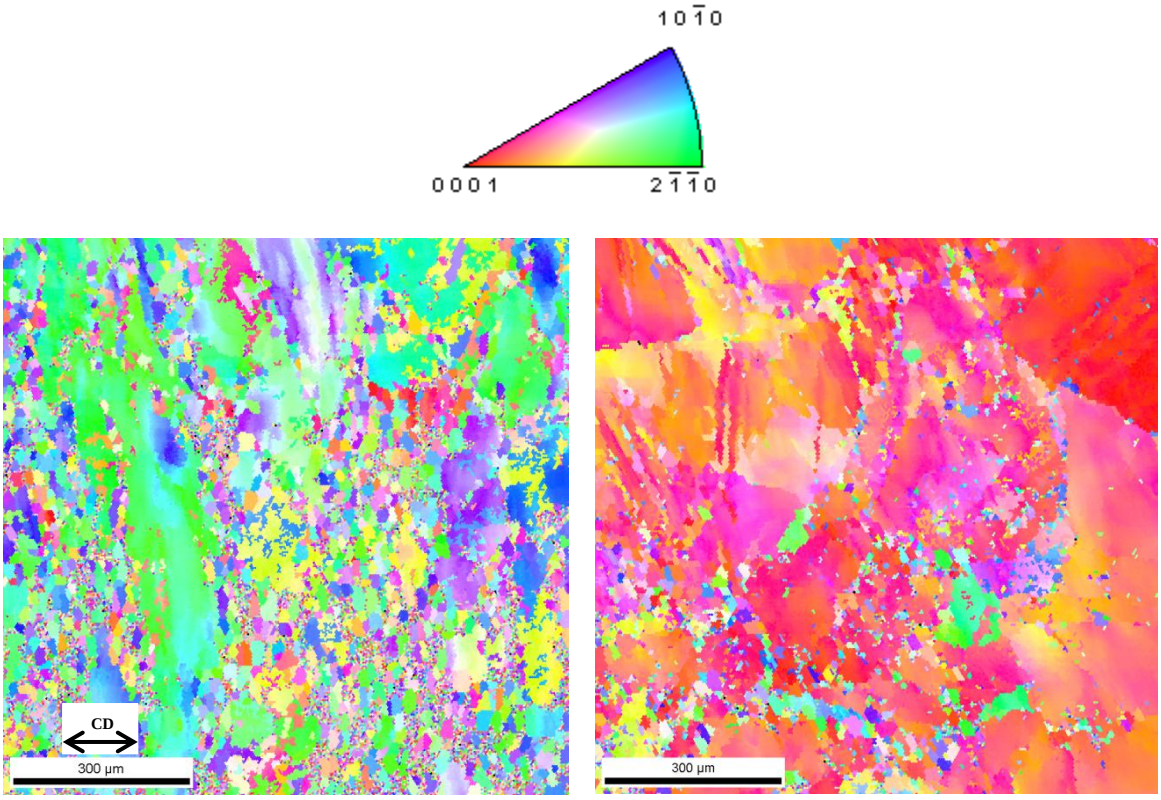

Figure 35: IPF maps showing crystal orientation of E20 samples deformed at 425°C and a strain rate of 0.01/s for a) longitudinal orientation and b) transverse orientation

These maps suggest that these newly formed grains are of multiple crystal orientations evidenced by the heterogeneous colors displayed. Additionally, the fine grain structure in these maps exhibit a grain diameter of approximately 10 microns closely correlating with the fine grain structures seen via LOM in Figure 14 and Figure 20. In each view the coarse grain structures in this samples tend to be preferentially aligned with newly nucleated grains showing no relationship to the origin coarse grain structure.

4. DISCUSSION

This analysis examines the formability based on the merit of compressive behavior of the magnesium alloys of various zinc compositions. For the duration of this discussion, formability and compressibility is used interchangeably. In this scope of this experiment, formability refers to the ability for the alloy to be deformed to the target strain without exhibiting any mechanical failure. Failure considered cracking, extreme oxidation, or any deformation-induced behavior which prevents the sample from retaining integrity from compression. This section will first present a basic interpretation of the compression performance of this alloy, and then expand a more in-depth understanding of the mechanisms at play during these deformations.

4.1 Formability assessment analysis

The formability assessment analysis demonstrated that there were definite trends the ZExx alloy system followed during compressive deformation. As an initial observation, it can be said that ZE20 was the most formable on the basis that it was able to withstand the largest range of temperatures from 200°C – 425°C and the largest range of strain rates from 0.01/s to 15/s without exhibiting failure as defined by this research. In all of these trial instances, ZE20 bars did not fail. The instance of failure (for either mode I or mode II) was much more frequent for ZE50 and ZE80. Initially, it appears that failure mode II became much more prevalent with more severe conditions. Severity is considered as approaching the upper extreme of each parameter selection (i.e. 425°C and 15/s).

4.1.1. Performance related to zinc content

From a preliminary analysis of these trials it appears that zinc content in each sample has the largest weight in influencing sample compressibility. This is based on the

trend that ZE20 was able to be deformed over a large array of temperature strain rate conditions while exhibiting no failures. Samples of ZE50 and ZE80, containing more zinc, were not able to be deformed at identical parameters without exhibiting failure. It is important to note for that all temperature and strain rate conditions, identical mechanical routines were used with the Gleeble thereby isolating zinc content (while neglecting minor environmental fluctuations) as the sole variable.

As a generalization, increasing zinc concentration increased the incidence of failure. This is evidenced as performance as a function of temperature and strain rate further degrades as zinc content increases from 2 wt.%, to 5 wt.%, and 8 wt.% in ZE20, ZE50, and ZE80 respectively. For example, ZE50 was able to be compressed without failure at some high strain rates while the ZE80 failure envelope is limited to strain rates less than 15/s. Explanations for zinc content influence are related to the effects of extended solid solution strengthening and boundary segregation (21) and will be discussed in a later portion of this study.

4.1.2. Performance related to strain rate

As a secondary factor, strain rate had an influence on the relative success of the compression trials but with not as much significance as zinc content. Strain rate influences are seen as an increased instance of failure across increasing severity (i.e. higher strain rates). Extremely low strain tests performed at 0.01/s were successful at a range of temperatures where higher strain analogues were not able to be deformed without failure. For all alloys, a the full range of temperatures able to be deformed with at least mixed successes at both extreme temperature conditions.

High strain conditions exhibited a much higher frequency of failures. Considering ZE50 and ZE80, in very few instances were compression bars able to be deformed at strain rates above 0.01/s. In the conditions in which trials passed, most generally the trials would pass over all strain rates, or the most extreme 15/s condition would fail. Reasoning for this can be attributed to fundamental strain rate behavior of alloys in which an increase of strain rate will commonly cause a more brittle fracture mode due to lack of time for dislocations to accommodate plastic flow of the material (22). Such behavior also means that a higher stress input is required to move a larger amount of bulk material in a shorter time span therefore submitting compression samples temporarily to a higher effective stress. This effect will be discussed in greater detail in later sections when the physical flow-stress behavior of the specimens is examined.

4.1.3 Performance related to temperature

Compression temperature also exhibits a secondary influence on the success of compression trials as compared to zinc content. In comparison to the effects seen by strain rate, temperature bears a similar if not more important influence on the compressibility of each test sample for given conditions. This generalization is seen best through two trends. First, pass/fail conditions show that for ZE50 and ZE80, higher temperature conditions exhibited a much higher instance of failure than did at low temperatures. Secondly, when high-strain failures occurred, failures would occur for most or all strain rates (1/s – 15/s) for a given temperature, indicating this parameter had a direct effect on the failure of the samples.

Such an effect can be considered from a thermodynamic scope when considering phase change effects in the ternary Mg – Zn – Ce system. Research was conducted by

Zhang, Luo, and Chang to develop a computational thermodynamic models of the Mg – Zn – Ce system. Isothermal ternary phase diagram projections from this research suggests as zinc increases, distance to the monovariant line of the matrix phase, α(Mg), suggesting a longer dwell time in a mushy zone region. More specifically, the liquidus temperature of the alloy system is decreased by increasing the zinc content. Figure 36 below shows a graphic representation of the fraction of solid versus the temperature, obtained through Scheil calculations. As this graph suggests, increasing zinc content reduces the fraction of solid, thereby increasing the probability of failure through temperature related mechanisms such as incipient melting (14).

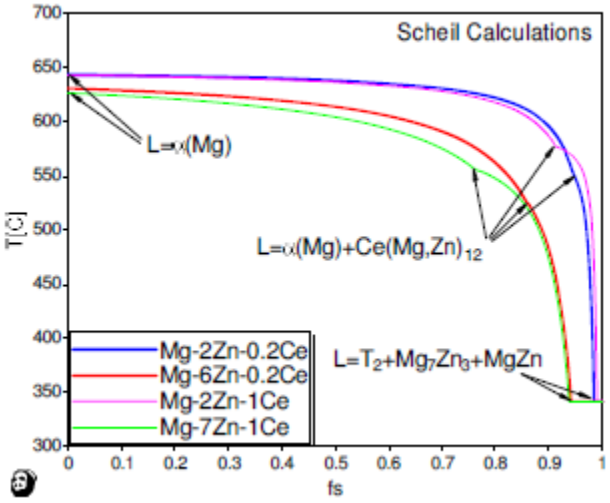

Figure 36: Schiel approximation representing fraction of solid as a function of temperature for varying zinc contents **(14)**

Since this study focused on a range of temperatures where liquid phase possible, incipient melting could be used to explain these failures. Figure 37 shows the binary Mg-Zn phase diagram.

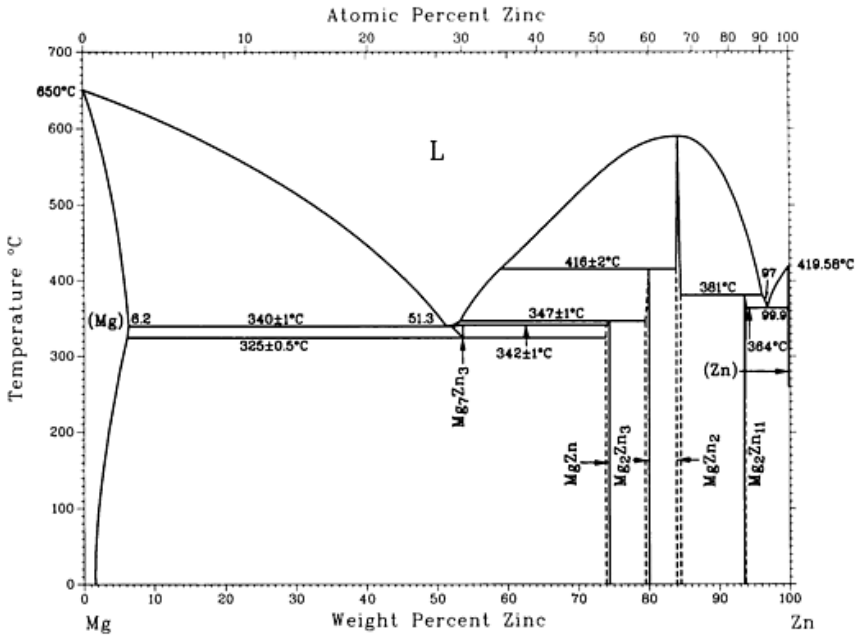

Figure 37: The binary Mg-Zn phase diagram **(27)**

As seen by the binary phase diagram, the regions of zinc content focus (2-8 wt.%) are commonly in a dual-phase α-Mg + liquid phase field at process conditions. Additionally, the first eutectic binary that forms between these two compounds occurs at 340°C. Considering this thermodynamic behavior, it is possible to have zinc melting within the scope of these thermo mechanical trials. Since liquid has no ability to support a stress, any fraction of molten material could contribute to compression failure (22).

As the occurrence of incipient melting is a possibility. This failure mechanism is strengthened by the instance of a mode II failure, as demonstrated in Figure 2a, which shows a failure akin to an intergranular failure. Subsequent metallographic and electron microscopy examinations are needed to verify this effect, and will be discussed in a subsequent portion of this study.

4.2 Flow-stress analysis

4.2.1. Curve interpretation

The compression curves were normalized so that the stress on the y-axis represents the uniaxial compressive engineering stress during compression based on an initial diameter of 8mm (a positive stress indicates compression). Not all curves exhibit a failure stress since compression failure mechanisms differ than uniaxial tension testing, and phenomena such as micro void coalescence, and microscopic events producing the necessary shear stresses to induce failure are not always present (22). In some instances compression bars were compressed to a strain of 0.8 with no failure.

It is important to note that the stress drop-offs at final strains are not actually failures, but the mechanical unloading portion of the test as compressive stress is removed from the system. Also notable is that there is no clear delineation of a compressive yield point that indicates the material transition from elastic to plastic behavior. There are several factors that could effect this, most likely is that the initial stress applied occurs at such a rate that the yield point cannot be resolved within the data output, shown as the extreme steep beginning regime of the flow-stress curve. Another explanation is that the material is extremely stiff and the elastic-plastic transition happens at such a low stress that it could not be resolved in these trials.

In low strain conditions these graphs exhibit a tendency to exhibit a portion of steady state behavior, followed by a regime exhibiting higher stresses at higher strains. This effect is due to the engineering interpretation of the flow-stress data. Material spreads during compression, which ultimately increases the cross sectional area of the specimen. As engineering flow-stress calculations do not account for cross sectional area

changes, the output strays from linearity. This effect is further intensified by the effect that material spreading during compression means that the compression specimen approaches a theoretical plane strain state in which, strain is constrained to one plane. In this condition, strain in the orthogonal conditions becomes more difficult as it nears a theoretically impossible state. A tertiary contributor to this effect is strain hardening increasing the material's resistance to plastic deformation, which can only be relieved by grain recovery.

Curves marked as failed show the ultimate stress at which fracture or severe surface cracking occurred. Sample failure initiated the breakdown of cohesion ultimately requiring little or no stress input after failure. The random nature of the flow-stress curves proceeding these failures represent material which is showing a lack of this aforementioned cohesion, or simply settling in the grips as the Gleeble continues to follow its programmed routine and articulate the compression jaws.

4.2.2. Performance related to test parameters

The flow-stress curves presented in Figure 3 through Figure 8 allow for the identification of several trends regarding the compressibility of each alloy in relation to the test parameters examined. Most notable is the effect that zinc content has on the performance of each alloy. Increasing the amount of zinc that is present in the system has a dramatic effect on the formability as established earlier in the pass/fail analysis of each compression bar. The alloy composition effect becomes even more evident when interpreting the data obtained from the flow-stress curves.

Considering flow-stress curves in which there was no specimen fracture, the generalization can be made that increasing the zinc content required less stress to deform to a specific strain. Such means that the value of the integral under the curve decreases indicating that overall energy input to the process is also at a minimum. However, the difference between the three alloy systems is not extremely drastic evidenced by for how a given strain each alloy falls within a stress range of approximately 25MPa.

As would be expected per conventional knowledge, increasing the strain rate of the alloy system requires higher stresses in order to deform to the same strains in lower strain rate situations. Such can be understood by interpreting the physical representation of the flow stress diagram. Since the integral of this graph represents input energy and the term energy is inversely dependent on time, time decreases impose energy increases. As such, more energy is needed to complete the same amount of deformation in a shorter time. This instantaneous increase in energy means that structure in the system may not be able to accommodate these imposed stresses.

Temperature reduces the necessary stress to deform a sample for various reasons. The first is the fundamental physical principal in regards atomic kinetic effects, and dislocation effects from heating. As more heat energy is put into the system, there is more energy available to deform bonds and promote dislocation motion. As more energy is available to the system, less is required to cause dislocation motion. Additionally, strain hardening which is taking place is elevated at some extent by temperature-induced recovery. These temperature effects are analogous to hot deformation techniques commonly used in industrial processing. To supplement this fundamental effect, magnesium formability is also aided by the activation of additional slip systems as

temperature is increased (10). By activating pyramidal slip systems, more slip planes are activated that would be able to accommodate imposed stress. Increasing the number of slip systems facilitated more deformation, manifesting as higher ductility.

4.3 Comparative metallographic analysis of various Mg-Zn-Ce samples

Metallographic specimens of ZExx revealed a wealth of information regarding the deformation behavior of Mg-Zn-Ce alloys. Grain size and general grain morphology can be used to determine the mechanisms which were influencing deformation in each alloy. Notably, large, deformed grain structures were visible at low energy inputs (low compression strain rates and low compression temperatures). Higher energy inputs (higher strain rates and higher temperatures) exhibited a higher degree of dynamic recrystallization (denoted DRX) in addition to deformed grain sections to be discussed further in this section.

Coarse grain structures were seen to facilitate deformation via twinning mechanisms. This can be seen in Figure 10 which show a large grain aspect ratio with a large degree of twinning within the boundaries. It was assumed that these are either tensile or compression twins originating from the basal slip system. Conversely, fine grain structures were seen in high energy parameters as per Figure 15. As stated earlier, it was assumed that these regions were capable of accommodating strain through various effects such as grain boundary sliding, twinning, and even the activation of pyramidal-type twinning if process temperature were high enough. The presence of each of these morphologies in samples that were successfully compressed suggests that there were different deformation mechanisms enabled either individually or simultaneously depending on the process parameters.

The morphology of DRX regions between ZE20 and ZE50 appeared differently. Grain coarsening can be seen between Figure 14 and Figure 18 in which the average grain size seen in ZE50 is larger than that in ZE20. Additionally, twinning was seen in ZE50 recrystallized grains, which was not seen in the ZE20 system. This structure tells two things about these fine grain regions. It first suggests that ZE50 grains underwent recrystallization first, as they are larger and had more time to coarsen following nucleation. The twinning within these grain regions then tells that the structure was still being deformed after their formation. Secondly, the more equiax and twin-free nature of the ZE20 fine grains suggest that they were nucleated closer to the end of compression. A possible explanation for this effect can be attributed to varying zinc content which affects the system's ability to undergo stable nucleation of grains; such would indicate either that zinc would be more likely to promote DRX effects, or higher concentrations somehow interact with Ce precipitates which are thought to contribute to particle stimulate nucleation effects (2). In either case, this evidence suggests that DRX regions are responsible for the accommodation of strain.

An interesting observation is that compressed samples at high temperatures and low strain rates exhibited a deformed grain texture as seen in Figure 10. In high strain rate and high temperature deformations there was a higher amount of energy input to each system. In each of these scenarios, new grain formation and relief via DRX could be seen by the fine grain structure which is much smaller than that of the starting material. This high-energy induced recrystallization suggests that there lies critical point where the energy input in the system induces nucleation of new strain-free grains in order to accommodate the high stresses being put on them and is also temperature dependent.

Similar behavior was seen in previous systems where a critical temperature of 400°C was suggested (28). Evidence from this study shows that when recrystallization occurred in a particular alloy such as ZE20, then the corresponding ZE50 and ZE80 either also showed signs of DRX or failed in compression. This suggests that DRX is a necessary mechanism to sustain deformation beyond these critical energies.

4.4 SEM analysis

4.4.1 Fracture mode identification of Mode II failures

SEM micrographs provide to be a powerful tool for use in fractography surfaces because they provide magnifications and depths of field that provide a large amount of rich, visual information. For this study, multiple levels of magnification were used to investigate several different regions of interest. Low magnifications were used in order to discern information that would suggest the fracture mode and mechanisms that influenced each failure. At higher magnifications, features of interest were related to the surface topography and physical texture details which could aide in understanding exactly the modes of failure.

Low magnification images taken suggest with reasonable confidence that the mode of fracture present in these samples was of the intergranular (IG) mode, initiating at the grain boundaries. This is evidenced by the grain-shape in Figure 23. The IG a mode can be promoted by various metallurgical and material factors such as incipient melting, phase segregation, or segregation of impurities and tramp elements to these boundaries. In this particular situation it is believed that reason for IG failure was due to zinc segregation to the grain boundaries, which will be further discussed during consideration

of spectroscopy data obtained from electron microscopy samples. An early indicator of this fact can be attributed to boundary zinc eutectic residence in Figure 26

Higher magnification images of the failure surfaces feature surface topography that exhibited a large amount of extension from the surrounding surface and appeared "spiked" as seen in Figure 24. These facets are indicative of ductile behavior. The spike tip develops as material deformation progresses, the material "holds on" to itself, plastically deforming until the cross-sectional area reaches a critical point where it is no longer able to bear the local stresses imposed on it. Surface undulations visible at magnifications of 2000X are likely due to roughly the same effect on a less severe scale.

The aggregate data obtained by observational analysis of the fracture surface is consistent with what could have happened during compression of samples that underwent failure. Assuming a perfectly lubricated interface of the compression bar, as the specimen was compressed, it strived to for volumetric conservation. In doing such, it was able to expand in the orthogonal directions in which it was not constrained. These radial strains bore the consequence of a radial stress which was capable of pulling grains apart in the IG mode. The intergranular nature of this fracture could have been due to either temperature effects inducing localized boundary melting, or stress concentrator proximity to boundaries. As separation continued, areas that were more adherent remained attached until they ultimately fractured causing the incidence of the spiked features. It is also important to note that these spikes were oriented in the orthogonal direction to the compression axis, conforming to this theory.

4.4.2 Interpretation of EDS chemical analysis

Chemical analysis conducted with EDS allowed for classification of structures that were seen in scanning electron microscopy. One discrete phase visible in the Mg-Zn-Ce system manifested as curved, lamellar structures which were confirmed to be some stoichiometric zinc intermetallic. Prior thermodynamic and transmission electron microscopy studies conducted by Zhang *et al.* showed that for these particular alloy systems, the Mg_7Zn_3 was commonly expected and often found to reside at the grain boundaries as a result of secondary eutectic formation (14). This study supported these claims by using the EDS mapping technique to show that the visible intermetallic phase was zinc-rich as seen in Figure 29. Figure 29 goes on to further support the claim of zinc common existence at the grain boundaries by commonly showing a morphology which is reminiscent of a grain boundary triple point. Though chemical analysis techniques used were not necessarily sensitive enough to confirm the identity of Mg_7Zn_3, it unequivocally showed boundary zinc, likely from a higher solutionized or precipitate presence at these localities.

The same study suggests the possibility of other structures, such as $CeMg_{12}$ and $CeZn_{12}$, being able to be formed through ternary interaction. In observation, cerium rich structures were able to be observed as in Figure 28 confirmed by Figure 30. Due to similar morphology and random occurrence, these structures could not be easily resolved from the dominant Mg-Zn structures. Furthermore, the EDS data shows incidence of Ce-based intermetallics was less frequent, mainly attributed to the low 0.2wt% concentration of cerium.

Generally, eutectic structure is expected at the grain boundaries as this is thermodynamically the most stable place for phase growth to occur. Such morphology

with the zinc eutectics observed suggest that these structures are secondary formation with the primary phase being α-Mg. One interesting feature of the zinc in this system is that even when it is not present as an individual, discernible intermetallic particle, it still tends to migrate to matrix phase grain boundaries. Figure 31 depicts an EDS map of a ZE20 test specimen. In this micrograph it is possible to see that the zinc map detected by EDS, exhibits more intense at grain boundaries. For the same field, intermetallic particles are not visible at the grain boundary which suggests that zinc exists in some solutionized form in the α-Mg matrix.

An understanding of these zinc resident structures at the grain boundaries is important because it can be used to further support suggestions of zinc directly having an influence on the failure mode of these alloys. Specifically, this provides an explanation for the IG failure modes that were seen in earlier fractography examinations. To verify this, a specimen which had fractured in mode I but had begun to show signs of IG failure was examined via SEM. The electron micrograph in Figure 26 clearly shows a high incidence of zinc at crack roots along grain boundaries suggesting that it serves as an initiator of IG failure.

All examinations in this study carry the implication that the effect of zinc bears a strong responsibility for compressibility of this material system. As such, a stronger correlation is made for local grain boundary fracture to be caused by zinc effects. To reiterate, the purpose of the alloying addition of zinc in this particular system is as a strengthening agent. Prior studies suggest that an excess of zinc leads to a solid solutions strengthening effect which ends up negating the ductility enhancement effects imposed by cerium. Chino *et al.* have shown evidence of this effect via identification of Zn

precipitation of stretch forming samples which exhibited decreased ductility with increasing zinc content (4).

The correlation of observations between zinc eutectic at the grain boundaries, dissolved zinc at the grain boundaries, and zinc residence at compression crack roots indicates that zinc has some influence on the failure of these samples. This suggestion is further supported by the increase in failure frequency and reduction of processing envelope as zinc content increased among the three alloys studied. The exact reasoning for these failures was not specifically determined, but there are two likely reasons: 1) the zinc eutectic structure exhibited a lower melting point than surrounding matrix and therefore contributed to incipient melting and 2) the migration of solutionized zinc to the grain boundaries contributes to excessive strengthening, thereby inducing a steep property gradient which causes the grain boundaries to become stress concentrators.

4.4.3 Grain texture analysis

EBSD orientation maps revealed great deal of information regarding the resultant structure of ZExx samples following compressive deformation. This data can indicate the tendency of the grain structure to react to imposed deformation. A bulk aligned crystal texture can reveal the deformation history of a wrought material and suggest that the material is energetically stable in that configuration. Randomized structure indicates that crystal orientation is likely not due to deformation therefore due to energy-activated mechanisms during deformation, or thermally-induced processes. In the case of an HCP crystal with limited slip system activation, EBSD can tell the potential for an alloy to deform according to a weak or strong basal texture.

An important observation in this research is that starting grain structure was randomized as seen in Figure 9. This data indicates that in the ZExx alloy system, effects of alloying elements are activated instantaneously causing a randomized grain structure whereas unalloyed magnesium tends to show a basal character (11). This structure is beneficial to compressive deformation as HCP crystal structures are commonly known to deform via the basal twinning mechanism (2; 9; 16; 8), Randomized grain orientation means that as-cast structures are able to facilitate deformation in a magnitude of directions. Specifically, even when deformation is constrained to one crystal direction via twinning, a heterogeneously-oriented polycrystalline structure can accommodate stress in more directions. As discussed prior, this randomized structure is thought to be an effect of cerium precipitates which nucleates new, randomized grains through particle stimulated nucleation (16).

Recrystallization was seen in various fields through fine grains and randomized crystal orientations. Fine grain structures which were evident in deformed samples were deemed to be randomized since the orientation, indicated by color on the IPF map, is random. This data correlates with prior light optical observations which suggest there is an increase in a grain refined zone due to DRX.

It is known DRX is important to the deformation of these alloys; two theories have been developed to explain the mechanisms at play. The first is that DRX randomizes crystal orientation, meaning that twinning can occur in new directions. By dynamically recrystallizing grains, the ZExx system was able to accommodate deformation in new crystallographic orientations that do not exhibit basal alignment (2). The second theory suggests that DRX is beneficial to the formability of Mg and its alloys

since they typically exhibit a great deal of grain boundary sliding (11). In a fine-grained material, the relative area of grain boundary is much higher meaning that the potential for deformation to occur in a myriad of directions is increased (28). As such, the potential for homogenous deformation was increased, and therefore the potential to deform in a more ductile manner was increased.

It is likely that the former, randomization mechanism, is much more applicable to this system. EBSD data of deformed samples which did not undergo DRX show preferred grain alignments. These structures deviate from the as-cast alloys as they are not random. This fact alone indicates that directionality is influenced by deformation and nucleation of new randomized orientations can aide in supporting additional strain. Furthermore, grain sliding would bear no relationship to DRX since samples were able to be deformed without developing refined grain regions.

5. CONCLUSIONS

Compression of the Mg-Zn-Ce alloy system was studied in order to classify the influence of strain rate, temperature, and zinc content during deformation. A multi-tool approach including mechanical data, metallographic analyses, and electron microscopy was used in order to develop explanations for mechanisms which were responsible for augmenting ductility in this system. The following conclusions were developed regarding the ZExx system:

1) Increasing zinc content in this system reduces the range of temperatures strain rates at which the alloy can be deformed by promoting the increase of surface cracking, oxidation and complete disintegration during deformation
2) Failures seen were of the intergranular mode and attributed to an increased zinc residence at the grain boundaries
3) A critical input energy exists which induces the recrystallization of the grain structure resulting in small equiaxed grains of heterogeneous crystallographic orientation

LIST OF REFERENCES

1. **United States Automotive Materials Partnership.** *Magnesium Vision 2020: A north american automotive strategic vision for magnesium.* s.l. : United States Council for Automotive Research, 2007.

2. *High-ductility magnesium-zinc-cerium extrusion alloys.* **A.A. Luo, R.K. Mishra, A.K. Sachdev.** 64, 2011, Scripta Materialia, pp. 410-413.

3. **C.J. Bettles, M.A. Gibson.** Current Wrought Magnesium Alloys: Strengths and Weaknesses. *JOM.* May 2005, pp. 46-49.

4. *Compressive devormation behavior at room temperature - 773 in Mg-0.2 mass%(0.035 at.%)Ce alloy.* **Y. Chino, M. Kado, M Mabuchi.** 56, 2008, Acta Materialia, pp. 387-394.

5. *The texture and anisotropy of magnesium-zinc-rare eath alloy sheets.* **J. Bohlen, M.R. Nurnberg, J.W. Senn, D. Letzig, A.R. Agnew.** 55, 2007, Acta Materialia, pp. 2101-2112.

6. *Research for a "new age of magnesium" in the automotive industry.* **H. Friedrich, S. Schumann.** 2001, Materials Processing Technology, Vol. 117, pp. 276-281.

7. *Extruded High-Strength Solid Materials Based on Magnesium with Zinc, Yttrium, and Cerium Additives.* **X. Guo, D. Shechtman.** 1, 2005, Glass Physics and Chemistry, Vol. 31, pp. 44-52.

8. *On the Nonbasal Slip in Magnesiunm Crystals.* **H. Yoshinaga, R. Hoiuchi.** 4, 1963, Transactions of the Japanese Institute of Metals, Vol. 5, pp. 14-21.

9. *Slip, Twinning, and Fracture in Hexagonal Close-Packed Metals.* **Yoo, M.H.** 1981, Metallurgical Transactions A, Vol. 12A, pp. 409-418.

10. *The influences of alloying additions and processing parameters on the rolling microstructures and textures of magnesium alloys.* **L.W.F. Mackenzie, M. Pekguleryuz.** 480, 2008, Materials Science and Engineering A, pp. 189-197.

11. *Influence of cerium on the texture and ductility of magnesium extrusions.* **R.K. Mishra, A.K. Gupta, P.R. Rao, A. K. Sachdev, A.M. Kumar, A.A. Luo.** 59, 2008, Scripta Materialia, pp. 562-656.

12. **Rokhlin, L.L.** *Magnesium Alloys Containing Rare Earth Metals.* London : Taylor and Francis, 2003.

13. *Experimental study of the Ce-Mg-Zn phase diagram at 350°C via diffusion couple techniques.* **D. Kevorkov, M. Pekguleryuz.** 478, 2009, Joyrnal of Alloys and Compounds, pp. 427-436.

14. *The solidification microstructure and precipitation investigation of magnesium-rich alloys containing Zn and Ce.* **C. Zhang, A.A. Luo, A. Chang.** 2011. Magnesium Technology 2011.

15. **A.A. Luo, R.K. Mishra, A.K. Sachdev.** *High ductility/strength magnesium alloys. 0116994 A1* USA, May 7, 2009.

16. *Development of High Ductility Magnesium-Zinc-Cerium Extrusion Alloys.* **A.A. Luo, R.K. Mishra, A. K. Sachdev.** 2010. Magnesium Technology 2010.

17. *Polycrystalline behavior analysis of pure magnesium by the homogenization method.* **Tadano, Y.** 2, 2010, International Journal of Mechanical Science, Vol. 52, pp. 257-265.

18. *The recrystallization and texture of magnesium-zinc-cerium alloys.* **L.W.F. Machenzie, M.O. Pekguleryuz.** 59, 2008, Scripta Materialia, pp. 665-668.

19. *Principles of equal-channelangularpressing as aprocessingtool for grainrefinement.* **R.Z. Valieva, T.G. Langdon.** 7, 2006, Progress in Materials Science, Vol. 51, pp. 881-981.

20. *Mechanism of Precipitation Hardening of Magnesium-Zinc Alloys.* **G. Mima, Y. Tanaka.** 5, 1971, Transactions of the Japan Institute of Metals, Vol. 12, pp. 317-322.

21. *Strengthening effect of Zn in heat resistant Mg-Y-Zn solid solution alloys.* **M. Suzuki, T. Kimura, J. Koike, K. Maruyama.** 48, 2003, Scripta Materialia, pp. 997-1002.

22. **Hertzberg, R.** *Deformation and Fracture Mechanics of Engineering Materials.* s.l. : J. Wiley and Sons, 1996.

23. *Influence of Zn concentration on stretch formability at room temperature of Mg-Zn-Ce alloy.* **Y. Chino, X. Huang, K. Suzuki, K. Sassa, M. Mabuchi.** 528, 2010, Materials Science and Engineering A, pp. 566-572.

24. **Dynamic Systems Incorperated.** Gleeble Operations Manual. Postenkill, NY : DSI.

25. *Effects of extusion ratio on the microstructure and mechnical properiteis of AZ31 Mg alloy.* **Y. Chen, Q. Wang, J. Peng, C. Zhai, W. Ding.** 182, 2007, Journal of Materials Processing Technology, pp. 281-285.

26. **Gerard, B.F.** *Investigating microstructural gradients and high strain rate deformation mechanisms in industrial magnesium alloy components.* Bethlehm : Lehigh University: Master Thesis, 2009.

27. **ASM International.** *Volume 3: Alloy Phase Diagrams.* s.l. : ASM International, 2012.

28. *Dynamic recrystallization and texture development during hot deformation of magnesium alloy AZ31.* **Y. Xu-Yue, J.I. Ze-sheng, H. Miura, T. Sakai.** 2009, Transactions of Nonferrous Metals Society of China, Vol. 19, pp. 55-60.

29. *EBSD Study on the Deformation Twinning in AZ31 Magnesium Alloy During Quasi-in-Situ Compression.* **H. Yang, S. Yin, C. Huang, Z. Zhang, S. Wu, S. Li, Y. Liu.** 10, 2008, Advanced Engineering Materials, Vol. 10, pp. 955-960.

30. *Dynamic recryustallization during high temperature deformation of magnesium.* **T. Al-Samman, G. Gottstein.** 2008, Materials Science and Engineering A, Vol. 490, pp. 411-420.

VITA

Andrew Thome was born on June 25th,1988 to his parents, Gail and Peter Thome. From birth, he resided in rural Newton, NJ where he attended Kittatinny Regional High School. In high school Andrew was constantly involved with extra-curricular activities while maintaining membership in the National Honor Society.

After high school graduation in 2006, Andrew attended Lehigh University where he connected with his freshman advisor, Wojciech Misiolek, who would go on to become his thesis advisor. At Lehigh, Andrew actively pursued his degree in materials science while becoming actively involved in other aspects of his professional field. After a summer internship with the Carpenter Technology Corporation in Reading, PA, he realized his interest in metallurgy. Andrew went on to focus his career through serving as the student materials society treasurer, working a second summer as an engineering intern and becoming avidly involved in his local ASM professional society. In 2009, he and fellow teammates were awarded 2nd place in a poster competition for the International Metallographic Society. Andrew received his B.S. in materials science and engineering on May 2010.

During graduate school, Andrew was awarded the Lowey Family Graduate Student Fellowship to pursue his studies. He maintained his affiliations with ASM serving as the executive committee member at large, the materials camp co-chairman, technical chairman for several chapter meetings, and on the exposition sub-committee. Andrew has written several conference papers regarding magnesium and aluminum alloys.